A quiet day empirical model of electron density of the Indian equatorial F-region at 500 km altitude

Article *in* Solar-Terrestrial Physics · March 2023

DOI: 10.12737/stp-91202308

3 authors:

Pradip Bhuyan
Dibrugarh University
186 PUBLICATIONS **2,530** CITATIONS
SEE PROFILE

Minakshi Chamua
Tinsukia College
15 PUBLICATIONS **133** CITATIONS
SEE PROFILE

Kalyan Bhuyan
Dibrugarh University
80 PUBLICATIONS **698** CITATIONS
SEE PROFILE

Solar-Terrestrial Physics. 2023. Vol. 9. Iss. 1. P. 68–72. DOI: 10.12737/stp-91202308. © 2023 M. Chamua, P.K. Bhuyan, K. Bhuyan. Published by INFRA-M Academic Publishing House

UDC 550.51
DOI: 10.12737/stp-91202308

Received April 06, 2022
Accepted January 19, 2023

A QUIET DAY EMPIRICAL MODEL OF ELECTRON DENSITY IN THE INDIAN EQUATORIAL F-REGION

M. Chamua
Tinsukia College, Department of Physics, Assam, India, mchamua@gmail.com

P.K. Bhuyan
Dibrugarh University, Department of Physics, Assam, India, pkbhuyan@gmail.com

K. Bhuyan
Dibrugarh University, Department of Physics, Assam, India,kalyanbhuyan@gmail.com

Abstract. In this paper, we present a quiet day empirical model of electron density (N_e) for the Indian equatorial zone at an altitude of 500 km. The model is applicable to all levels of solar activity and is based on the observation that the electron density in the F-region of the Indian zone is correlated with the $F10.7$ cm solar flux at each local time and in every month. Using this characteristic, we describe the model for electron density. In this model, we have used the least square fit and the polynomial fit. The electron density measured by the Retarding Potential Analyzer (RPA) on board the SROSS C2 satellite from 1995 to 2000 and FORMOSAT-1 (ROCSAT-1) satellite, operated by the National Space Organization (NSPO, now the Taiwan Space Agency (TASA)) of the Republic of China (Taiwan), from 1999 to 2004 is used to derive the relationship between N_e and $F10.7$. The average altitudes of SROSS-C2 and FORMOSAT-1 are 500 km and 600 km respectively. Due to this height difference, the observed data obtained by FORMOSAT-1 is normalized to match the SROSS-C2 data. The model is compared with the observations and is found to be in good agreement with them. It is applicable to quiet ($A_p < 15$) conditions and is limited to a fixed altitude of 500 km within the latitude range of 10° S to 10° N around the 75° E meridian.

Keywords: equatorial ionosphere; modeling; solar activity cycle; mathematical and numerical techniques.

INTRODUCTION

In order to illustrate the properties of the ionosphere and improve prediction capabilities, empirical models of electron density, electron temperature, ion temperature, critical frequency of F2 layer (f_oF2), peak height of F2 layer (h_mF2), etc. are very important. A large number of station-specific, regional, and global models of ionosphere based on in-situ measurements, incoherent scatter radar (ISR) measurements, middle and upper atmosphere (MU) radar measurements, etc. have been developed. An excellent review of many available empirical models has been presented by Bilitza [2002] (see also references therein). Among those models are the International Reference Ionosphere (IRI) [Bilitza, 1990, 2001], which was developed and periodically uploaded, and the International Union of Radio Science (URSI), which is the most widely used model. One empirical model providing the electron density profile is the N_e Quick model [Radicella, Zhang, 1995; Radicella, Leitinger, 2001; Leitinger et al., 2005]. Empirical models created using Incoherent Scatter Radar data are Millstone Hill (42.6° N, 288.5° W) [Holt et al., 2002] in the United States, Saint Santin [Zhang et al., 2004] in France (44.6° N, 2.2° E), Shigaraki (the MU radar site) [Zhang et al., 2007] in Japan (34.8° N, 136.1° E), Arecibo (18.3° N, 66.7° W) [Zhang et al., 2007] in Puerto Rico.

Ionization and peak density as represented by ionospheric total electron content (TEC) and N_mF2 normally exhibits a linear relationship with solar activity measured in terms of the 10.7 cm solar flux index $F10.7$ and the sunspot number R_z. However, there have been a number of reports which indicate that the linear relationship does not hold well near solar maximum, i.e. for very high values of $F10.7$ [Titheridge, 1978; Bhuyan et al., 1983; Lakshmi et al., 1988; Kane, 1992; Rishbeth, 1993]. Balan et al. [1993, 1994] have shown that during intense solar cycle 21 when $F10.7$ frequently exceeded 300 and reached a maximum value of 367, TEC and related $F10.7$ increased nonlinearly. The observed nonlinear variation of ionization density with solar flux has been theoretically investigated by Balan et al. [1994] using the Sheffield University Plasmasphere Ionosphere model. The relative importance of neutral winds, neutral densities, and solar EUV fluxes in the observed nonlinear phenomenon has been explored. It has been found that the saturation of ionization is caused by the saturation of production of ionization due to the nonlinear increase in solar EUV fluxes while nonlinear increase in neutral density seems to have no effect on the saturation. In other words, the ionosphere (and atmosphere) responds linearly to solar EUV (or UV) inputs and $F10.7$. Using SROSS C2 and FORMOSAT-1 data, we have found a linear relationship between the electron density N_e and the $F10.7$ cm solar flux from solar minimum to maximum of solar cycle 23. In this paper, we have derived a model of N_e for $A_p < 15$ based on the best linear positive correlation between N_e and $F10.7$. We have used SROSS C2 data for the period 1995–2000 and FORMOSAT-1 data for the period 2001–2003 to derive this quiet day model. The model has been developed using all data in between ±10° magnetic latitude for $A_p < 15$ over the Indian subcontinent.

DESCRIPTION OF THE MODEL

Using the best correlation between N_e and $F10.7$, we present a model of the electron density in this paper. In this model, we have used the least square fit and the polynomial fit. The model is a quiet day model (A_p<15), and it operated from 1995 to 2003 at an average altitude of 500 km. The latitude range of the model is 10° S to 10° N around the 75° E meridian. Since the average altitude of the satellite FORMOSAT-1 was 600 km, we have normalized the FORMOSAT-1 N_e data to the altitude to match it with the SROSS C2 data. For the period 1999–2000, we have both SROSS-C2 and FORMOSAT-1 data. In solar cycle 23, the $F10.7$ cm flux varied from a minimum of 69 to a maximum of 237, and solar activity was not so intense. The yearly average $F10.7$ values for 1999, 2000, 2001, 2002, 2003, and 2004 are approximately 143, 182, 185, 178, 129, and 107 respectively. Solar activity during the period 1999–2004 varies from moderate to slightly high levels. Therefore, for the period 1999–2000, we have calculated the electron density difference for an altitude difference of 100 km. This electron density difference was subtracted from the electron density obtained from the FORMOSAT-1 data at the peak of solar cycle 23.

The modeled density can be obtained from the following equation:

$$N_e = mf + c, \quad (1)$$

where f is the monthly mean $F10.7$ cm solar flux, N_e is the monthly mean electron density for the current month; m and c are given by the following equations:

$$m = a_1 l^4 + a_2 l^3 + a_3 l^2 + a_4 l + a_5, \quad (2)$$

$$c = b_1 l^4 + b_2 l^3 + b_3 l^2 + b_4 l + b_5, \quad (3)$$

where l=0, 1, 2, …, 23 is the local time. Since we have found the polynomial fit as the best, we use the polynomial approximation in local time.

The coefficients a_1, a_2, and b_1, b_2 are given in Table 1 for each of three seasons: summer, winter, and equinoxes. Coefficients are calculated for each season from monthly mean $F10.7$. We can calculate the modeled electron density for each month and for all levels of solar activity (low, medium, and high) over the Indian equatorial zone from monthly mean $F10.7$. For all summer months, the coefficient will be same, but monthly mean N_e for each local time is calculated from monthly mean $F10.7$. The same procedure is performed for the other seasons.

MODEL RESULTS AND VERIFICATIONS

Figure 1 shows superimposed plots of modeled and observed (SROSS-C2 and FORMOSAT-1) electron densities as function of local time for June, December, March, and September for three levels of solar activity: low (left panel), moderate (middle panel), and high (right panel). The daytime electron density starts increasing after sunrise becomes maximum at 12:00–15:00 hrs. The observed and modeled electron densities at noon are listed in Table 2 for comparison. The nighttime electron density is underestimated by the model for all levels of solar activity and all seasons. For low solar activity, the model gives negative electron density values for nighttime. Table 3 shows the observed and modeled values at 02:00 hr for comparison. Since this model is a regional model for the Indian region at the altitude of 500 km, the modelled data could not be compared with the electron density obtained from other satellites such as ISR or SWARM as they cannot provide N_e for all local times over the Indian zone. Therefore, the model presented in this paper cannot be compared with observations from other satellites.

Table 1. Coefficients a_1, a_2, and b_1, b_2, or each of the three seasons: summer, winter, and equinoxes

	Summer	Winter	Equinoxes
a_1	$0.0082 \cdot 10^8$	$0.0072 \cdot 10^8$	$0.0089 \cdot 10^8$
a_2	$-0.4518 \cdot 10^8$	$-0.3949 \cdot 10^8$	$-0.4933 \cdot 10^8$
a_3	$7.4041 \cdot 10^8$	$6.5785 \cdot 10^8$	$8.3164 \cdot 10^8$
a_4	$-31.299 \cdot 10^8$	$-29.429 \cdot 10^8$	$-38.353 \cdot 10^8$
a_5	$42.719 \cdot 10^8$	$54.987 \cdot 10^8$	$63.024 \cdot 10^8$
b_1	$0.0036 \cdot 10^{10}$	$0.0047 \cdot 10^{10}$	$0.003 \cdot 10^{10}$
b_2	$-0.2184 \cdot 10^{10}$	$-0.2406 \text{x} 10^{10}$	$-0.1819 \cdot 10^{10}$
b_3	$3.9022 \cdot 10^{10}$	$3.7718 \cdot 10^{10}$	$3.3411 \cdot 10^{10}$
b_4	$-17.859 \cdot 10^{10}$	$16.097 \cdot 10^{10}$	$-16.68 \cdot 10^{10}$
b_5	$27.46 \cdot 10^{10}$	$34.233 \cdot 10^{10}$	$37.847 \cdot 10^{10}$

DISCUSSION

The regional and global empirical models of the ionosphere that have been developed so far across the world are based on various mathematical and numerical techniques. The St. Santin incoherent scatter radar models [Zhang et al., 2004] and the Millstone Hill ISR models [Holt et al., 2002] have been created using a bin-fit technique. Liu et al. [2008] have designed an empirical model for the ionospheric propagation factor M (3000) F2 based on the empirical orthogonal function analysis method. Jain et al. [1996], Bhuyan and Baruah [1996], Unnikrishnan et al. [2002] have applied the harmonic analysis to regional empirical modeling of the ionospheric electron content (IEC) over Lunping (25° N and 121.2° E), f_oF2 over India, and TEC over Palehua respectively. Oyama et al. [2004] have developed an empirical model for electron temperature, using measurements on board the Hinotori satellite; the model is based on spline-approximation of measured electron temperature T_e in 5-dimentional space comprised of solar activity $F10.7$, month of the year, local time, geographic longitude, and geomagnetic latitude. Bhuyan and Chamua [2006] have presented an empirical model of T_e for the Indian equatorial and low latitudes using SROSS C2 RPA measurements; it is based on the regression analysis.

In this paper, we present a quiet day empirical model of electron density over the Indian zone, using the least square fit and the polynomial fit technique. Comparison between the model and the observed data shows that the model reproduces most of the features seen in measured electron density. For example, the daytime peak density

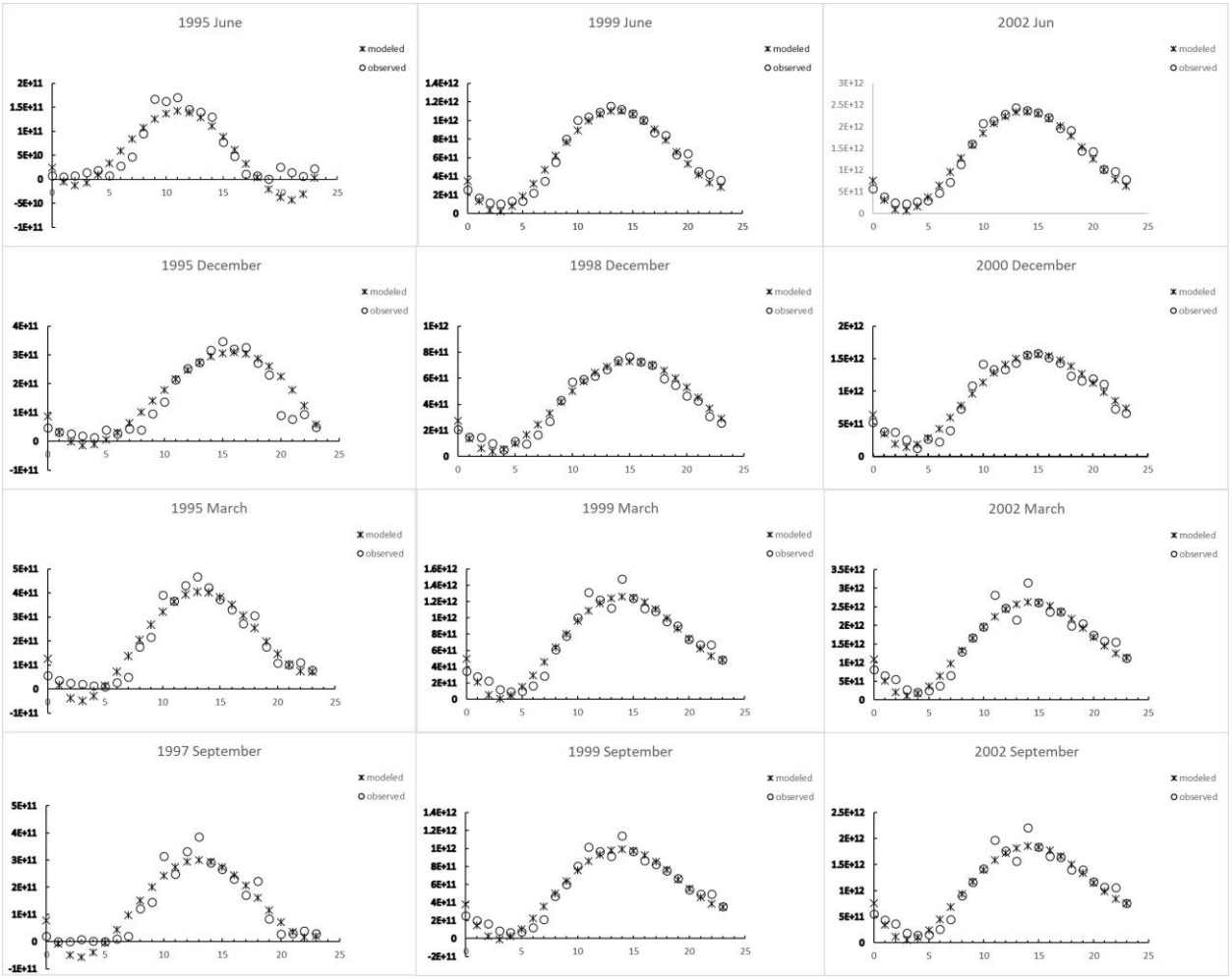

Figure 1. Superimposed plots of modeled and observed electron densities as function of local time for low (left panel), moderate (middle panel), and high (right panel) solar activity

Table 2: Observed and modeled electron densities at noon

Months	Low solar activity		Moderate solar activity		High solar activity	
	observed	modeled	observed	modeled	observed	modeled
June	$1.45\cdot10^{11}$	$1.39\cdot10^{11}$	$1.09\cdot10^{12}$	$1.06\cdot10^{12}$	$2.29\cdot10^{12}$	$2.24\cdot10^{12}$
December	$2.53\cdot10^{11}$	$2.53\cdot10^{11}$	$5.94\cdot10^{11}$	$5.78\cdot10^{11}$	$1.34\cdot10^{12}$	$1.41\cdot10^{12}$
March	$4.31\cdot10^{11}$	$3.93\cdot10^{11}$	$1.22\cdot10^{12}$	$1.18\cdot10^{12}$	$2.46\cdot10^{12}$	$2.43\cdot10^{12}$
September	$3.32\cdot10^{11}$	$2.94\cdot10^{11}$	$9.69\cdot10^{11}$	$9.33\cdot10^{11}$	$1.76\cdot10^{12}$	$1.73\cdot10^{12}$

Table 3. Observed and modeled electron densities at 02:00 hr

Months	Low solar activity		Moderate solar activity		High solar activity	
	observed	modeled	observed	modeled	observed	modeled
June	$7.61\cdot10^{9}$	$-1.30\cdot10^{10}$	$1.14\cdot10^{11}$	$3.42\cdot10^{10}$	$2.50\cdot10^{11}$	$2.94\cdot10^{11}$
December	$2.74\cdot10^{10}$	$-1.41\cdot10^{10}$	$1.45\cdot10^{11}$	$6.45\cdot10^{10}$	$3.76\cdot10^{11}$	$1.93\cdot10^{11}$
March	$2.56\cdot10^{10}$	$-3.82\cdot10^{10}$	$2.28\cdot10^{11}$	$2.56\cdot10^{11}$	$5.50\cdot10^{11}$	$2.05\cdot10^{11}$
September	$1.4\cdot$	$-4.99\cdot10^{10}$	$1.64\cdot10^{11}$	$2.61\cdot10^{10}$	$3.68\cdot10^{11}$	$1.21\cdot10^{11}$

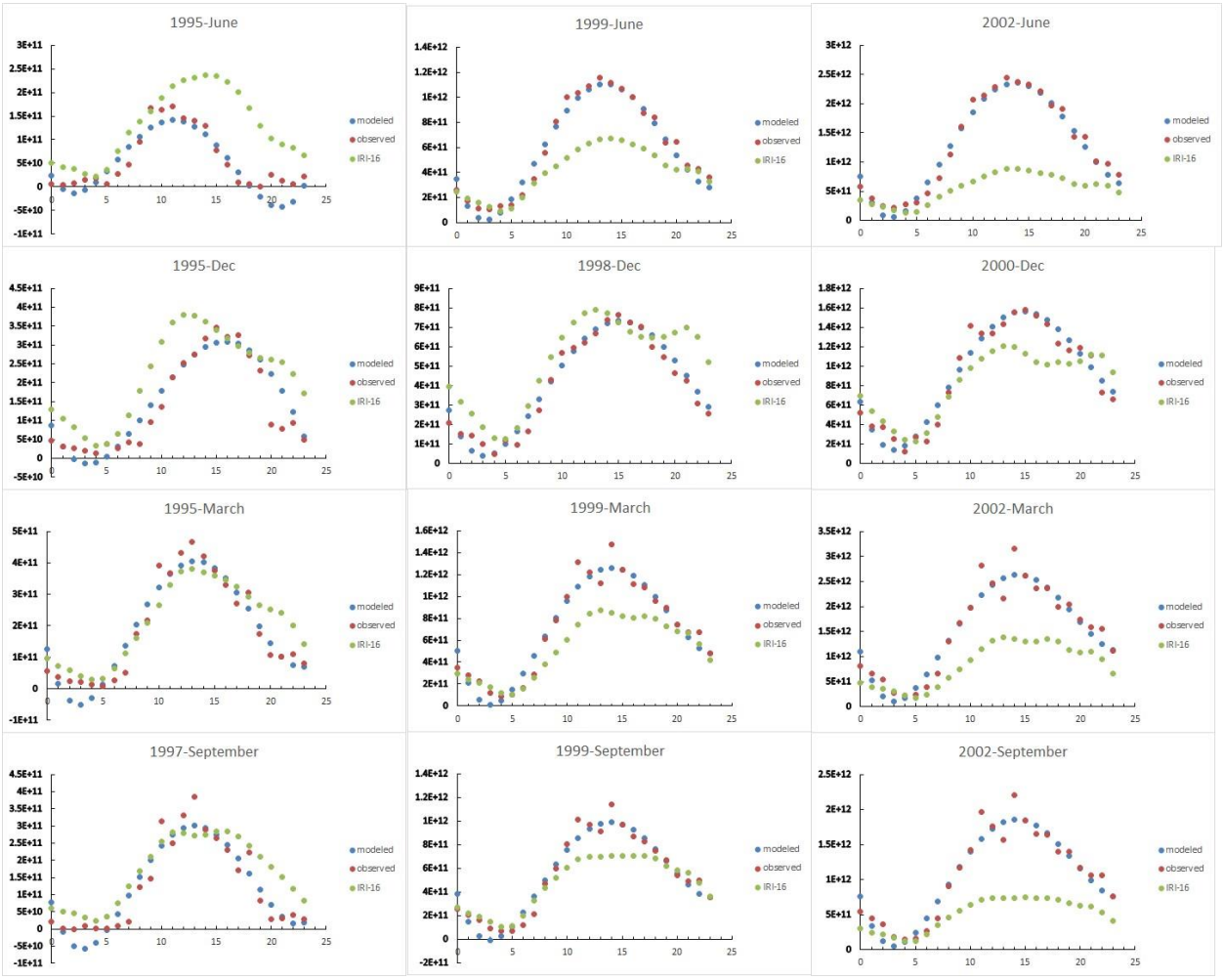

Figure 2. Comparison of the observed and modeled data with IRI-16 (International Reference Ionosphere-16) model for low (left panel), moderate (middle panel) and high (right panel) solar activity

occurs around 13:00 hr in summer and equinoxes, while in winter the peak density occurs two hours later at ~15:00 hr. However, the nighttime modeled electron densities are very low compared to the observed N_e during low solar activity for all seasons.

Figure 2 compares the observed and modeled data with IRI-16 (International Reference Ionosphere-16) model for all the three levels of solar activity, for summer, winter, and equinox months. From the figure it is seen that during low solar activity except for the equinox months and daytime (10:00–15:00 hrs) IRI overestimates observed and modeled electron densities for all local times. For moderate solar activity except for the winter month, the daytime electron density is underestimated by IRI for summer and equinox months. At 14:00 hr, IRI underestimates observed and modeled N_e by about 40 % in June, by about 43 % in March, and by about 38 % in September. During high solar activity, the daytime electron density is underestimated by IRI for summer, winter, and equinox months, whereas during nighttime IRI underestimates N_e for summer and equinox months, but overestimates it in the winter month.

At 14:00 hr, IRI underestimates N_e by about 28 % in December, by 62 % in June, by 57 % in March, and by 66 % in September. In December, N_e predicted by IRI-16 shows an evening enhancement for low, medium, and high solar activity. Also in December, the daytime maximum density occurs around 15:00 hr in case of observed and modeled data, whereas IRI predicts daytime maximum density around 13:00 hr.

CONCLUSION

The electron density measured at ~500 km by the SROSS C2 satellite from 1995 to 2000 and at ~600 km by the FORMOSAT-1 satellite from 2001 to 2004 is used to derive an empirical model of electron density applicable to the Indian equatorial and low-latitude regions. It is based on the observation that the electron density in the F-region of the Indian equatorial and low-latitude ionosphere has positive correlation with the $F10.7$ cm solar flux.

The empirical model described in this paper is successful in reproducing the daytime electron densities for all season and all levels of solar activity. However, the nighttime electron density is underestimated by the model for all levels of solar activity and for all months. The drawback of the model is that it gives negative electron density values for low solar activity at nighttime.

Except for the equinox months, the IRI overestimates observed and modeled electron densities for all

local times for low solar activity. During moderate solar activity, IRI underestimates the observed and modeled daytime electron densities in June, March, and September and overestimates them in December. At high solar activity, the daytime electron density is underestimated by IRI for all the four months, i. e. June, December, March, and September. IRI overestimates the nighttime electron density in December and underestimates it in June, March, and September. Bhuyan et al. [2003] have reported that IRI overestimates N_e at nearly all local times and in all seasons for low solar activity.

This model can be used as a regional alternative for electron density for almost full solar cycle. Nonetheless, the model has some limitations. It is limited to the fixed altitude of 500 km within the latitude range of 10° N to 10° S around the 75° E meridian and is applicable to quiet conditions ($A_p < 15$). Since the International Reference Ionosphere cannot correctly predict N_e over the Indian subcontinent, the empirical model described in this paper can be incorporated in IRI for accurate prediction of the electron density over this region. This model can be helpful in developing an ionospheric map over the Indian subcontinent with the aid of other available resources such as the International Reference Ionosphere (IRI) model, other observed data over the region at different altitudes. The ionospheric map depicting accurate values of h_mF2 and f_oF2 along with the electron density profile at any location over the Indian subcontinent will be a useful tool for high frequency (HF) communications and space weather applications.

Authors wish to express their sincere thanks to National Space Organization (NSPO) for the FORMOSAT-1 data.

REFERENCES

Balan N., Bailey G.J., Jayachandran B. Ionospheric evidence for a non-linear relationship between the solar EUV and 10.7 cm fluxes during an intense solar cycle. *Planet. Space Sci.* 1993, vol. 41, pp. 141–145. DOI: 10.1016/0032-0633(93)90043-2.

Balan N., Bailey G.J., Jenkins B., Rao P.B., Moffett R.J. Variations of ionospheric ionization and related solar fluxes during an intense solar cycle. *J. Geophys. Res.* 1994, vol. 99, pp. 2243–2253. DOI: 10.1029/93JA02099.

Bhuyan P.K., Baruah S. A regional mapping of the f_oF2 over India as an additional input to IRI. *Adv. Space Res.* 1996, vol. 18, no. 6, pp. 205–208. DOI: 10.1016/0273-1177(95)00924-8.

Bhuyan P.K., Chamua M. An empirical model of electron temperature in the Indian topside ionosphere for solar minimum based on SROSS C2 RPA data. *Adv. Space Res.* 2006, vol. 37, pp. 897–902. DOI: 10.1016/j.asr.2005.09.016.

Bhuyan P.K., Tyagi T.R., Singh L., Somayajulu Y.V. Ionospheric electron content measurements at a northern low midlatitude station through half a solar cycle. *J. Radio and Space Phys.* 1983, vol. 12, pp. 84–93.

Bhuyan P.K., Chamua M., Bhuyan K., Subrahmanyam P., Garg S.C. Diurnal, seasonal and latitudinal variation of electron density in the topside F-region of the Indian zone ionosphere at solar minimum and comparison with the IRI. *J. Atmos. Solar-Terr. Phys.* 2003, vol. 65, iss.3, pp. 359–368. DOI: 10.1016/S1364-6826(02)00294-8.

Bilitza D. International Reference Ionosphere. Rep. NSSDC/WDC-R&S 90-22. *World Data for Rockets and Satellites*. National Space Science Data Centre. Greenbelt, Md. 1990.

Bilitza D. International Reference Ionosphere 2000. *Radio Sci.* 2001, vol. 36, iss. 2, pp. 261–275. DOI: 10.1029/2000RS002432.

Bilitza D. Ionospheric models for radio propagation studies. *Rev. Radio Sci. 1999–2002*. edited by W.R. Stone, IEEE and Wiley. 2002, pp. 625–679.

Holt J.M., Zhang S.-R., Buonsanto M.J. Regional and local ionospheric models based on Millstone Hill incoherent scatter radar data. *Geophys. Res. Lett*. 2002, vol. 29, no. 8. DOI: 10.1029/2002GL014678.

Jain S., Vijay S.K., Gwal A.K. An empirical model for IEC over Lunping. *Adv. Space Res.* 1996, vol. 18, no. 6, pp. 263–266. DOI: 10.1016/0273-1177(95)00935-3.

Kane K.P. Solar cycle variation of f_oF2. *J. Atmos. Terr. Phys*. 1992, vol. 54, pp. 1201–1218. DOI: 10.1016/0021-9169(92)90145-B.

Lakshmi D.R., Reddy B.M., Dabas R.S. On the possible use of recent EUV data for ionospheric predictions. *J. Atmos. Terr. Phys*. 1988, vol. 50, no. 3, pp. 207–213. DOI: 10.1016/0021-9169(88)90069-4.

Leitinger R., Zhang M.L., Radicella S.M. An improved bottomside for the ionospheric electron density model NeQuick. *Ann. Geophys*. 2005, vol. 48, no. 3, pp. 525–534. DOI: 10.4401/ag-3217.

Liu C., Zhang M.-L., Wan W., Liu L., Ning B. Modeling M (3000) F2 based on empirical orthogonal function analysis method. *Radio Sci.* 2008, vol. 43, RS1003. DOI: 10.1029/2007RS003694.

Oyama K.-I., Marinov P., Kutiev I., Watanabe S. Low latitude model of T_e at 600 km based on Hinotori satellite data. *Adv. Space Res*. 2004, vol. 34, pp. 2004–2009. DOI: 10.1016/j.asr.2004.07.013.

Radicella S.M., Zhang M.L., The improved DGR analytical model of electron density height profile and total electron content in the ionosphere. *Ann. Geophys*. 1995, vol. 38 (1), pp. 35–41. DOI: 10.4401/ag-4130.

Radicella S.M., Leitinger R. The evolution of the DGR approach to model electron density profiles. *Adv. Space Res.* 2001, vol. 27, no. 1, pp. 35–40. DOI: 10.1016/S0273-1177(00)00138-1.

Rishbeth H. Day-to-day ionospheric variations in a period of high solar activity. *J. Atmos. Terr. Phys*. 1993, vol. 55,iss. 2, pp. 165–171. DOI: 10.1016/0021-9169(93)90121-E.

Titheridge J.E. The electron content of the southern midlatitude ionosphere, 1965–1971. *J. Atmos. Terr. Phys*. 1978, vol. 35, iss. 5, pp. 981–1001. DOI: 10.1016/0021-9169(73)90077-9.

Unnikrishnan K., Nair R.B., Venugopal C. Harmonic analysis and an empirical model for TEC over Palehua. *J. Atmos. Solar-Terr. Phys.* 2002, vol. 64, no. 17, pp. 1833–1840. DOI: 10.1016/S1364-6826(02)00187-6.

Zhang S.-R., Holt J.M., Zalucha A.M. Midlatitude ionospheric plasma temperature climatology and empirical model based on Saint Santin incoherent scatter radar data from 1966 to 1987. *J. Geophys. Res. Lett.* 2004, vol. 109, A11311. DOI: 10.1029/2004JA010709.

Zhang S.-R., John M.H., Bilitza D.K., Eyken T.V., Mc Geady M., Amory-Mazaudier C., Fukao S., Sulzer M. Multiple-site comparisons between models of incoherent scatter radar and IRI. *Adv. Space Res.* 2007, vol. 39, no. 5, pp. 910–917. DOI: 10.1016/j.asr.2006.05.027.

How to cite this article:

Chamua M., Bhuyan P.K., Bhuyan K. A quiet day empirical model of electron density in the Indian equatorial F-region. *Solar-Terrestrial Physics*. 2023. Vol. 9. Iss. 1. P. 68–72. DOI: 10.12737/stp-91202308.

Bull. Mater. Sci. (2022) 45:220
https://doi.org/10.1007/s12034-022-02801-6

Role of concentration on $Cd_xPb_{1-x}S$ thin films: synthesis, characterization and photovoltaic cells properties

LIPIKA GOGOI[1,*], JITUPON GOGOI[2], RUPKAMAL CHETIA[2], MINAKSHI CHAMUA[3], SURAJIT KONWER[2] and PRASANTA KUMAR SAIKIA[1]

[1]Department of Physics, Dibrugarh University, Dibrugarh 786004, India
[2]Department of Chemistry, Dibrugarh University, Dibrugarh 786004, India
[3]Department of Physics, Tinsukia College, Tinsukia 786125, India
*Author for correspondence (lipikagogoi5@gmail.com)

MS received 19 April 2022; accepted 10 July 2022

Abstract. The $Cd_xPb_{1-x}S$ thin films with different concentrations of x from 0.2 to 0.8 were synthesized using the chemical bath deposition method. X-ray diffraction (XRD) and Williamson–Hall (W–H) plot gives the crystallite size that decreases with increased concentration. XRD, high-resolution transmission electron microscopy and selected area electron diffraction patterns of the film samples evidence the hexagonal phase structures of both CdS and PbS. Energy-dispersive X-ray confirmed the presence of Cd, Pb and S in the film samples. The transmittance of the film samples increases with the increase in concentration. Optical studies show the prominent blue shift in bandgap energy, whereas the Urbach energy decreases with the increased concentration x. The electrical conductivity of the films at room temperature is of the order of 10^{-5} $(\Omega cm)^{-1}$. The efficiency of the heterojunction cell structures $Cd_xPb_{1-x}S$/CdTe and $Cd_xPb_{1-x}S$/CdSe are calculated to be 3.37 and 2.21%, respectively.

Keywords. $Cd_xPb_{1-x}S$; XRD; HRTEM; Urbach energy; electrical conductivity; photovoltaic cell.

1. Introduction

The continuously increasing demand for energy requires the exploration of non-fossil resources of energy, especially solar energy [1]. The uses of crystalline silicon solar cells are controlled besides having good efficiency because of their high cost [2]. This reason led to the idea of the development of cost-efficient solar cells. The materials' properties and preparative conditions highly affect the efficiency and stability of solar cells [3]. In recent times, the II-IV-VI group ternary compound appeared to be a promising material for optoelectronic applications [4]. Lead sulphide (PbS) is an essential IV–VI group compound semiconductor with a narrow bandgap of $\sim$0.41 eV, large exciton Bohr radius of $\sim$18 nm, and has optical absorption coefficient $>10^5$ cm^{-1} [5,6]. By the effective mass model, the optical bandgap of PbS can be tuned by modifying the crystallite size over the spectrum range from near-infrared to visible region [7–9]. When PbS is alloyed with suitable dopants like Zn, Cu, Gd, Cd, Bi, Sb, tunable electrical and optical properties can be achieved [10,11]. PbS has many applications in many fields such as photography, infrared detection, solar absorbers, gas sensors, diode lasers, humidity and temperature sensors, and solar control coatings [12,13].

On the other hand, an n-type II–VI semiconductor CdS with a wide bandgap of $\sim$2.46 eV is one of the primary characterized materials for window layer in solar cells due to its thermal and chemical stability, high refractive index and efficient transport properties [14]. CdS exhibit quantum size effects having a small Bohr exciton radius of $\sim$3 nm [15]. Under solar light irradiation conversion, CdS can be used for photoinduced redox [16]. CdS can be studied under several configurations: bulk materials, thin films, nanowires, nanorods, tetrapod nanocrystals, etc. [17]. Because of these remarkable properties, CdS have many applications in light-emitting diodes, photocatalytic, transistor and solar cells, etc. [18,19]. Considering the applications of CdS and PbS, and CdS and PbS are susceptible to light, the study of the mixed $Cd_xPb_{1-x}S$ thin film structure is of technical importance. CdS are used as a window layer in conventional solar cells, and PbS has used an absorber layer. Nonetheless, the tuning of optical bandgap energy and electrical conductivity by alloying PbS with Cd would result in better performance of $Cd_xPb_{1-x}S$ as a window layer in the solar cell.

In the present study, the chemical bath deposition (CBD) method has been embraced to deposit $Cd_xPb_{1-x}S$ thin films on glass substrates. Due to its simple routine, low cost, high efficiency and ability to deposit uniform films, CBD becomes an expedient method than the other synthesis

Published online: 02 November 2022

techniques [20–24]. A limited research work has been addressed for $Cd_xPb_{1-x}S$ thin films, with a symmetric variation of deposition parameters. Nair *et al* [25] have investigated the effect of Cd/Pb atomic% on the structural, optical and electrical properties of CdPbS films by changing the molarity of the precursors used for the preparation of the films by CBD technique. Forostyanaya *et al* [26] reported chemically deposited cadmium sulphide thin film in an aqueous solution of lead acetate $Pb(CH_3O_2)_2$. Deo *et al* [27] have prepared $Cd_{0.5}Zn_{0.5}S$ thin films by CBD method to investigate the structural, morphological and optical characteristics as a function of temperature. Anbarasi *et al* [28] have fabricated CdS:Pb thin films that were successfully fabricated on glass substrates by a spray technique using a perfume atomizer with different concentrations of Pb (0, 2, 4, 6 and 8 wt%). Barote *et al* [3] have studied the Photoelectrochemical performance of $Cd_{1-x}Pb_xS$ ($0 \leq x \leq 1$) thin films. Authors have discussed the influence of Cd content on the structural and optical properties of $Cd_xPb_{1-x}S$ thin films in their earlier work, Gogoi *et al* [29]. In that work, authors have successfully fabricated $Cd_xPb_{1-x}S$ thin films by the CBD method as a function of different Pb:Cd ratios. By changing Cd content in the host films, the transmittance as well as bandgap of the films enhanced, which makes the nanocrystalline films suitable candidate for photovoltaic cells as a window layer.

In these aforementioned research work, the application of $Cd_xPb_{1-x}S$ thin films as a window layer in photovoltaic cell have not been reported extensively. Therefore, it is necessary to study the photovoltaic response of the $Cd_xPb_{1-x}S$ thin films. The authors have explored the structural, morphological, optical and electrical properties of $Cd_xPb_{1-x}S$ thin films prepared at different concentrations on glass substrates in the present work. Because of the unique properties of indium tin oxide (ITO), like high optical transparency, low density of pinholes, low sheet resistance and low roughness, they become excellent transparent conducting oxide material used as a front contact in solar cell devices [30]. In our present study, we have used CdTe and CdSe as absorbing materials. Recent studies show that CdTe, CdSe, CdS, the Cd-based chalcogenide semiconductors are extensively used in many optoelectronic device applications such as photovoltaic cells, detectors, sensors, LED, etc. [31–33]. Among them, CdTe-based thin-film photovoltaic cells have recently exhibited the lowest cost of electricity for the utility of solar energy generation [34]. CdTe is one of the most potential absorber materials with a bandgap of 1.45 eV and has high direct optical absorption above $>10^4$ cm^{-1} [35,36]. CdSe is another considerable absorbing material with a suitable optical bandgap of 1.74 eV, and high absorption coefficient of 10^5 cm^{-1} in the visible spectra [37]. However, by employing the chloride treatment to the absorber layer, the solar cells' photovoltaic properties such as efficiency and stability can be improved [37–40]. Therefore, in the present work, the various photovoltaic parameters such as conversion efficiency, fill factor, open-circuit voltage and short circuit current of $Cd_xPb_{1-x}S$/CdTe and $Cd_xPb_{1-x}S$/CdSe photovoltaic cells fabricated with the ITO-$Cd_xPb_{1-x}S$ window layer were analysed with the help of the current–voltage (*J–V*) characteristic curve.

2. Experimental

2.1 *Materials and synthesis of $Cd_xPb_{1-x}S$ thin films*

$Cd_xPb_{1-x}S$ thin films are deposited onto chemically cleaned glass substrates at different concentrations, $x = 0.2$, 0.4, 0.6 and 0.8 M. First, 5 ml of cadmium acetate [$Cd(CH_3COO)_2{\cdot}2H_2O$] (99.9% pure) as Cd source and 5 ml of lead acetate [$Pb(CH_3COO)_2{\cdot}2H_2O$] (99.9% pure) as Pb source was used in a glass beaker. Then as an S source, 0.5 M of 5 ml thiourea [CH_4N_2S] (98% pure) was used in this mixed solution of Cd and Pb. Liquor ammonia [NH_3] (25%) was used to maintain the solution's pH at 12.0. Triethanolamine (TEA), 3%, was used as a complexing agent in the reaction. The deposition temperature of the chemical bath was maintained at 60°C for 120 min all throughout the process. The prepared films are yellow in colour. All the chemicals were of analytical grade and used without any further refinement. Deionized water was used as a common solvent to dissolve the chemicals at room temperature.

2.2 *Fabrication of heterojunction photovoltaic cells*

In the present work, $Cd_xPb_{1-x}S$/CdTe and $Cd_xPb_{1-x}S$/CdSe photovoltaic cells were fabricated with a superstrate configuration, shown in figure 1. $Cd_xPb_{1-x}S$ is used as a window layer, which is selected from the optimum conditions obtained from the films' characterizations of all the samples. In this investigation, the substrate is the ITO-coated glass plate (resistivity <10 Ohms $sq.^{-1}$). For absorber layer, cadmium telluride [CdTe] (99.9% pure) and cadmium selenide [CdSe] (99.9% pure) of sigma-Aldrich was used.

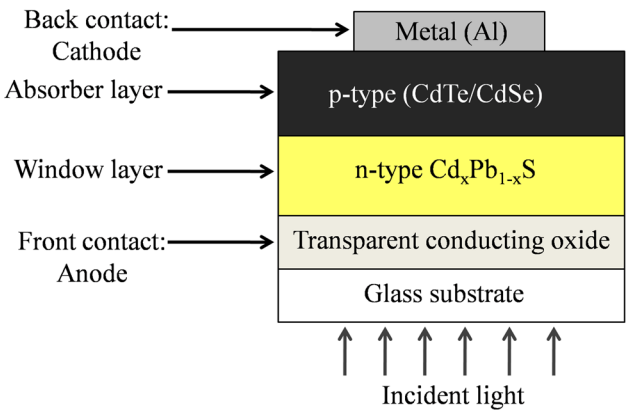

Figure 1. Standard superstrate configuration of heterojunction photovoltaic cell.

Aluminium [Al] was used as a back contact of the heterojunction photovoltaic cells.

A layer of CdTe or CdSe was deposited on the ITO/$Cd_xPb_{1-x}S$ coated glass substrate using the thermal evaporation technique on the top at a base pressure of $<10^{-6}$ mbar. CdTe powder, 0.6 g, was evaporated from a molybdenum boat by supplying ~4.4–4.7 A. The duration of the deposition was ~25 min, and deposited films were dark black in colour. Again, CdSe films were deposited by 0.6 g of CdSe powder evaporated from a molybdenum boat by supplying ~4.4 – 4.7 A. The duration of the deposition was ~40 min, and the prepared films were dark black in colour. Before making the back contact, CdTe and CdSe were treated with $CdCl_2$ with a 20% molar concentration at 200°C in a tube furnace for 1 h under ambient conditions. After $CdCl_2$ treatment, CdTe and CdSe were etched in a mixture of nitric acids and phosphoric acid to avoid unwanted oxide formation. Finally, a layer of Al was deposited on the top as a back contact by the thermal evaporation technique at a pressure of $<10^{-6}$ mbar. The device had an area of 1×1 cm^2 and was found stable for several months.

2.3 *Characterization*

X-ray diffractometer (XRD) [Model: Phillips X'Pert Pro] using CuKα radiation (λ = 1.5406 Å) as a source was used to determine the crystal structure of the deposited powder sample. Transmission electron microscope (TEM) images, high-resolution transmission electron microscopy (HRTEM) images and selected area electron diffraction (SAED) pattern were obtained using transmission electron microscope (TEM) [Model: JEOL JEM-2100] operated with an acceleration voltage of electron beam ~200 kV. Surface morphology and the chemical composition of the prepared films were obtained by using scanning electron microscope (SEM) [Model: JEOL JSM-IT 300] equipped with energy-dispersive X-ray (EDX) spectroscopy attachment. Fourier-transform infrared spectroscopy (FTIR) spectra were obtained using FTIR Spectrometer [Model: IMPACT 410] with software OMNIC E.S.P.5.0 to investigate the chemical bonding structure of the $Cd_xPb_{1-x}S$ thin films. The prepared films thickness was estimated by the Tolansky method using the Green line (λ = 5461Å) of Mercury. For optical studies, transmission spectra were recorded using a UV-Vis spectrophotometer [Model: Shimadzu UV-Vis 1800] in the wavelength range of 200 to 1100 nm. A Keithley source meter [Model: 2400:1] measured the films' current–voltage (I–V) characteristics graphs for electrical conductivity studies. The current–voltage (J–V) characteristics graphs of the fabricated photovoltaic cells were measured by a Keithley source meter [Model: 2400:1] under sun illumination intensity.

3. Results and discussion

The schematic presentation for the synthesis of $Cd_xPb_{1-x}S$ thin films is shown in figure 2. The details of the concentration parameters, along with the sample codes are listed in

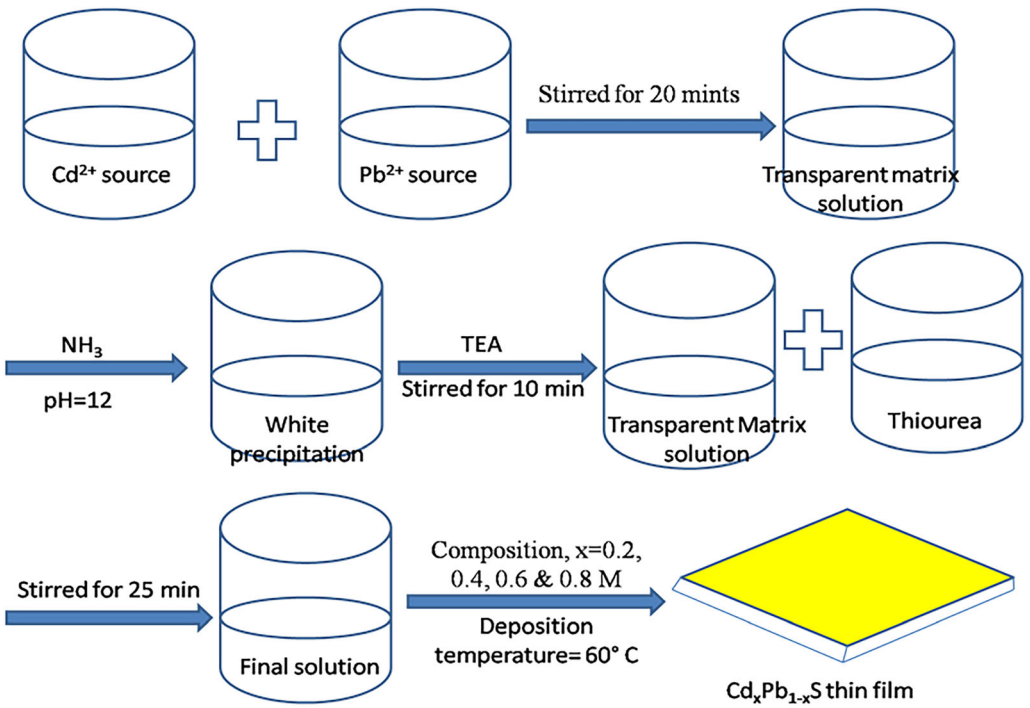

Figure 2. Schematic presentation for the synthesis of $Cd_xPb_{1-x}S$ thin films.

Table 1. Sample details of all the prepared $Cd_xPb_{1-x}S$ thin films.

Sample code	Volume	Molarity of thiourea	Concentration, x (M)
S_1	5 ml	0.5 M	0.2
S_2			0.4
S_3			0.6
S_4			0.8

table 1. The samples are coded as S_1, S_2, S_3, and S_4, respectively.

3.1 *Structural studies*

The XRD patterns of the $Cd_xPb_{1-x}S$ thin film samples S_1, S_2, S_3 and S_4 synthesized at different concentrations, x = 0.2, 0.4, 0.6 and 0.8 M, respectively, shown in figure 3. From the well-defined peaks of the diffraction pattern, the crystalline nature of the films is observed. The peaks that occurred at 2θ of 20.65°, 23.85°, 29.08°, 31.61°, 34.77° and 41.61° match with the planes (110), (111), (200), (112), (211) and (113), respectively, which can be indexed to tetragonal PbS [JCPDS card no.: 20-0596]. The peaks those arise at 2θ of 24.80°, 26.50°, 28.18°, 43.68°, 51.82° and 54.58° can be indexed to the planes (100), (002), (101), (110), (112) and (004), respectively, of hexagonal CdS [JCPDS card no.: 41-1049]. Although the number of peaks decreases with the increased x, in the case of S_4, one more additional peak has been observed at 38.58° indexed to the plane (102) of hexagonal CdS [JCPDS card no.: 41-1049], which is absent in the other three samples. Comparing the peak positions (2θ values) of XRD spectra with the standard

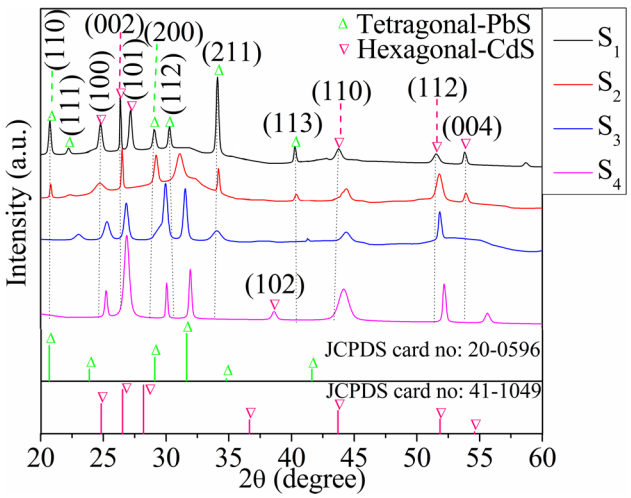

Figure 3. XRD diffraction patterns of $Cd_xPb_{1-x}S$ thin film samples S_1, S_2, S_3 and S_4 for different concentrations, x = 0.2, 0.4, 0.6 and 0.8 M, respectively. Green patterns and pink patterns represent the standard phases of tetragonal–PbS and hexagonal–CdS, respectively.

JCPDS data shows that all the film samples have been assigned to the phase structures of tetragonal PbS and hexagonal CdS, exhibiting the polycrystalline nature. The interplanar spacing 'd' decreases with the increase in concentration. When the x increases, the position of the diffraction peaks is shifted to the higher 2θ angle side. The difference in ionic radii of Cd^{2+} [41], Pb^{2+} [42] and S^{2+} [43] cause the shifting in peak position on the higher side [44].

The average crystallite size (D) of the $Cd_xPb_{1-x}S$ film samples is estimated by using Scherrer's equation [45]. Here, crystalline silicon has been used as standard reference material for position calibration and instrumental broadening calculation. The average crystallite size of the samples S_1, S_2, S_3 and S_4 is found to be ~40, 34, 27 and 20 nm, respectively. There is an increase in heterogeneity of the films for the concentration change in the host lattice. A gradual decrease of the crystallite size was observed, which was manifested by peak broadening and a slight shift of the position of the peaks towards the greater 2θ values. Also, the gradual increase of Cd concentration sequentially reduces the concentration of Pb in the host lattice. At the same time, the substitution of Cd^{2+} ions of smaller radius (0.91 Å) with Pb^{2+} ions of larger radius (1.48 Å) shrinks the host $Cd_xPb_{1-x}S$ crystal lattice. This causes a reduction in crystallite size. The values of the average crystallite size are shown in table 2.

The ascendancy of crystallite size and the internal strain on the XRD line broadening was estimated by X-ray peak profile analysis using Williamson–Hall (W–H) method [46]. The dissemblance between size-induced and strain-induced peak broadening is calculated using the W–H method by appraising the peak broadening as a function of 2θ [47]. In all crystallographic directions, the strain is presumed isotropic and is given as [48],

$$\varepsilon = \frac{\beta_T}{4\tan\theta}, \tag{1}$$

where ε is the lattice strain, β values are different for each peak for a multiple-ordered diffraction pattern of a film sample. In addition to Scherrer's equation and internal strain, W–H suggested for peaks as [29],

$$\beta_T \cos\theta = 4\varepsilon \sin\theta + \frac{K\lambda}{D}. \tag{2}$$

Equation (2) stands for the uniform deformation model (UDM). The straight line fitted in the graph between $\beta_T\cos\theta$ and $4\sin\theta$ represents the W–H plots. W–H plots for all the film samples for S_1, S_2, S_3 and S_4 are shown in figure 4a to d, respectively. The average crystalline size and strain were estimated from the intercept, and the slope of the linear fitted W–H plots is listed in table 2. The crystallite size of the film samples diminishes with the increase in x as concentration, while strain increases. The presence of positive slopes in the plot (figure 4a and c) indicates the possibility of tensile strain [49], whereas the appearance of negative

Table 2. Structural parameters, average crystallite size and strain of $Cd_xPb_{1-x}S$ thin films.

Sample code	Interplanar Spacing, d (Å)	Plane	Scherrer's method, crystallite size, D (nm)	*W–H* analysis (UDM)	
				Crystallite size, D (nm)	Strain, ε ($\times 10^{-3}$)
S_1	4.2867	110	40	41	2.12
	4.0028	111			
	3.6850	100			
	3.3830	002			
	3.2854	101			
	3.0742	200			
	2.9546	112			
	2.6312	211			
	2.2403	113			
	2.0703	110			
	1.7744	112			
	1.7042	004			
S_2	4.2734	110	34	36	3.62
	3.9873	111			
	3.6079	100			
	3.3659	002			
	3.0600	200			
	2.8790	112			
	2.6246	211			
	2.2348	113			
	2.0433	110			
	1.7665	112			
	1.7017	004			
S_3	3.8254	111	27	22	6.98
	3.5354	100			
	3.3257	002			
	3.0479	200			
	2.8398	112			
	2.6152	211			
	2.0425	110			
	1.7649	112			
S_4	3.5241	100	20	15	9.82
	3.3215	002			
	2.9754	200			
	2.8045	112			
	2.3335	102			
	2.0424	110			
	1.7539	112			
	1.6535	004			

slopes in the plot (figure 4b and d) indicates the presence of compressive strain [50]. The variation of crystallite size calculated from both Scherrer's and W–H methods, with variable x, is shown in figure 5.

To further study the crystallite size, structure of the prepared samples, TEM, HRTEM image and SAED patterns were recorded. The TEM image of sample S_2 is shown in figure 6. The inset of figure 6 represents the estimation of the corresponding particle size distribution histogram. The average crystallite size of the sample S_2 among 51 particles is $\sim$31 nm. The bright-field image of the sample S_2 (x = 0.4 M) corresponding SAED pattern is shown in figure 7a. The SAED pattern with distinguishable spots divulges that the sample S_2 is well-crystalline. The discerned three lattice planes are (110), (200) and (211), which correspond to tetragonal PbS (JCPDS: 20-0596). The other three lattice planes (002), (110) and (112) are associated with hexagonal CdS (JCPDS: 41-1049). The HRTEM image of the sample S_2 and its two arbitrary selected enlarged areas, which depict the clear lattice fringes indicating crystalline nature, is shown in figure 7b. The lattice spacing value for the sample S_2 is $\sim$0.332 nm for both the selected areas, which correspond to the (002) lattice plane of the CdS hexagonal phase (JCPDS: 41-1049). The results of TEM, HRTEM and SAED patterns of S_2 accorded with the XRD outcome for sample S_2.

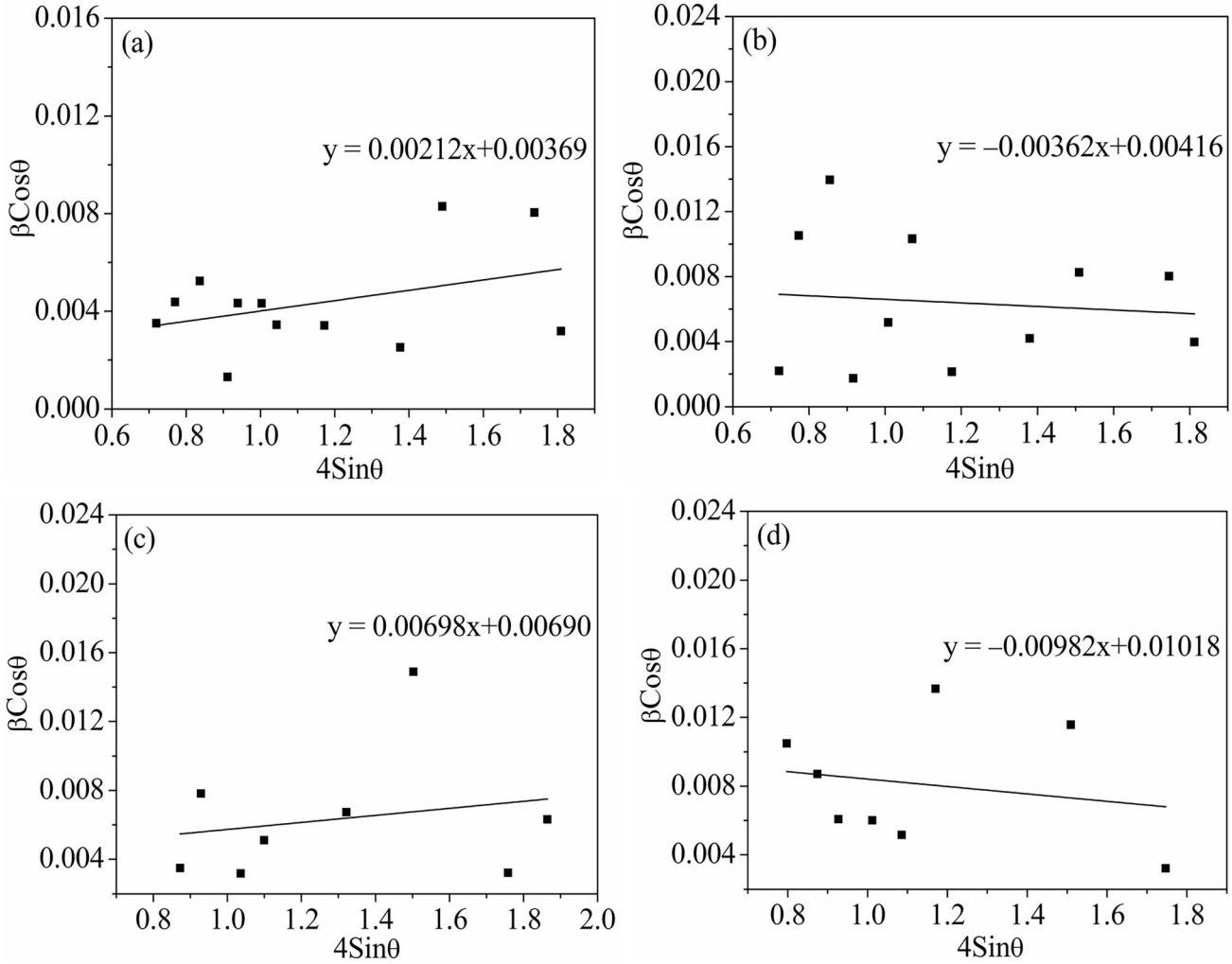

Figure 4. W–H plots of $Cd_xPb_{1-x}S$ thin film samples prepared at different concentrations of x assuming UDM: (**a**) S_1 (0.2 M), (**b**) S_2 (0.4 M), (**c**) S_3 (0.6 M) and (**d**) S_4 (0.8 M), respectively.

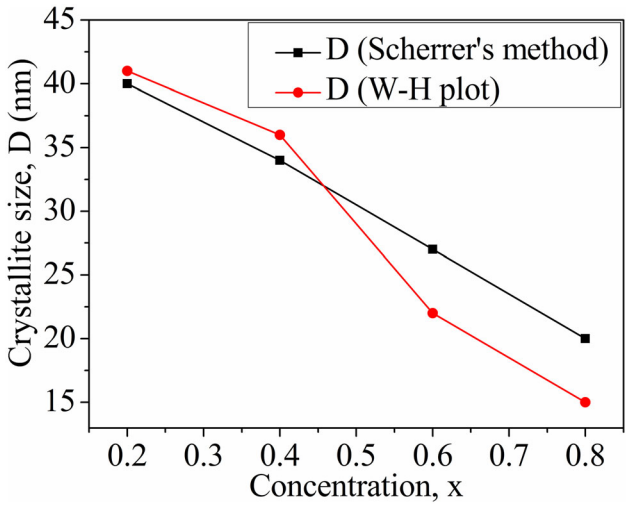

Figure 5. Variation of crystallite size calculated from both Scherrer's method and W–H plots with concentration x.

The TEM image of the sample S_4 is shown in figure 8. The estimation of the corresponding particle size distribution histogram is shown in the inset of figure 8. The average crystallite size calculated for the sample S_4 among 64 particles is ~22 nm. The result concurred with the result obtained from the XRD analysis for sample S_4. Figure 9a shows the bright-field image of the sample S_4 (x = 0.8 M) corresponding SAED pattern. The perceived five lattice planes (100), (002), (110), (112) and (004) correspond to the hexagonal CdS phase (JCPDS: 41-1049). In the S_4 sample, only one lattice plane (200) was observed that is associated with the tetragonal phase of PbS (JCPDS: 20-0596). The SAED pattern with clearly distinguishable diffraction spots designates the presence of polycrystalline structure in sample S_4. Furthermore, The HRTEM image of sample S_4 and its three arbitrary selected enlarged areas that portray clear lattice fringes signify its crystalline nature, shown in figure 9b. The HRTEM image of the sample

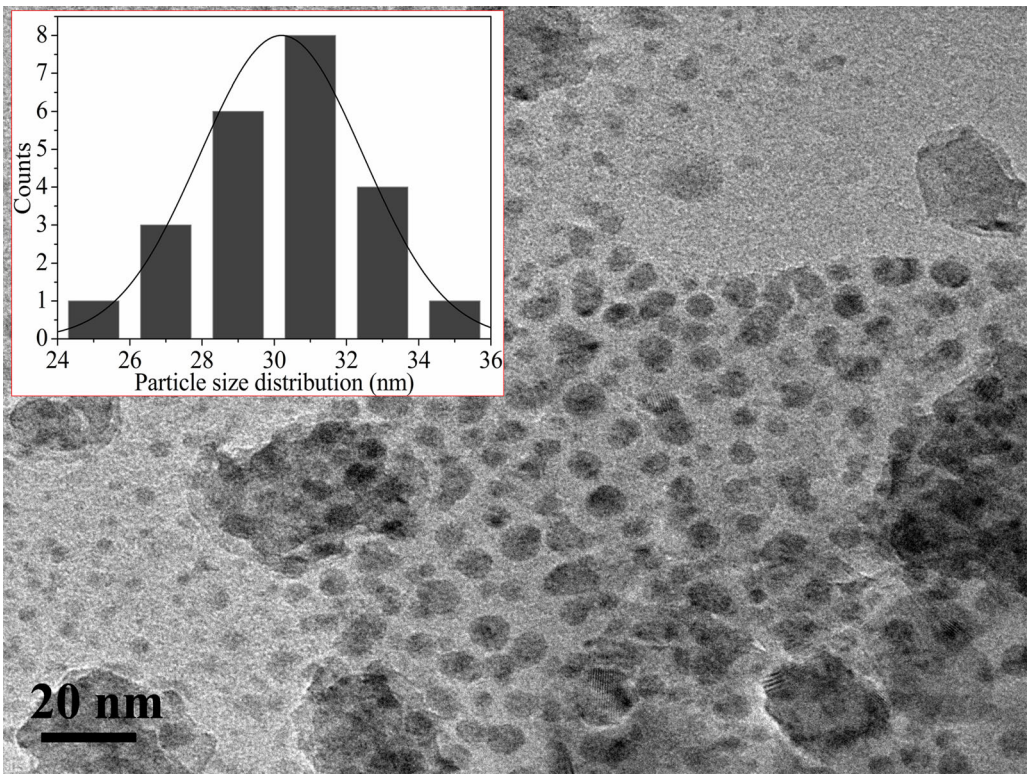

Figure 6. TEM image of the sample S_2 (0.4 M). The inset shows the corresponding particle size distribution histogram of the sample S_2.

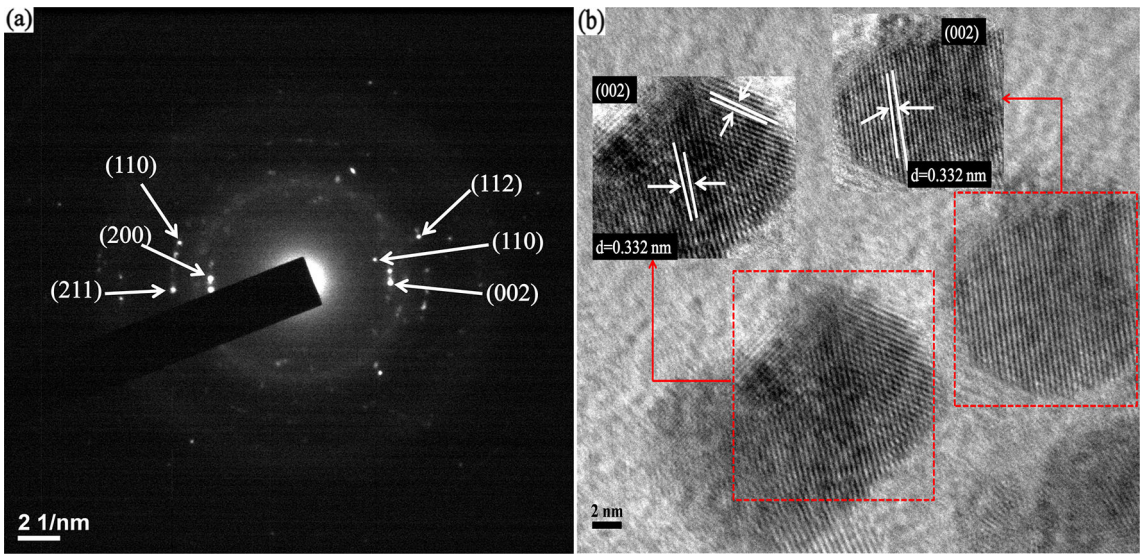

Figure 7. (**a**) The SAED pattern and (**b**) HRTEM image of sample S_2.

S_4 confirms the spacing value of ~0.196 nm for all three selected areas. It is consistent with the lattice plane (110), indexed to the hexagonal CdS phase (JCPDS: 41-1049). For sample S_4, the result of the TEM, HRTEM and SAED patterns are confirmed by XRD studies. The crystallite size, interplanar spacing and crystal planes for the samples S_2 and S_4, estimated from the TEM, HRTEM and SAED pattern, are listed in table 3.

3.2 *Morphological and concentrational studies*

SEM micrograph is used to study the morphology and particle size of the $Cd_xPb_{1-x}S$ thin-film samples. The morphologies and corresponding particle size distribution histograms of the samples: S_1–S_4 prepared at different concentrations, x, are shown in figure 10a–h, with the magnification of X10,000. The surface morphology

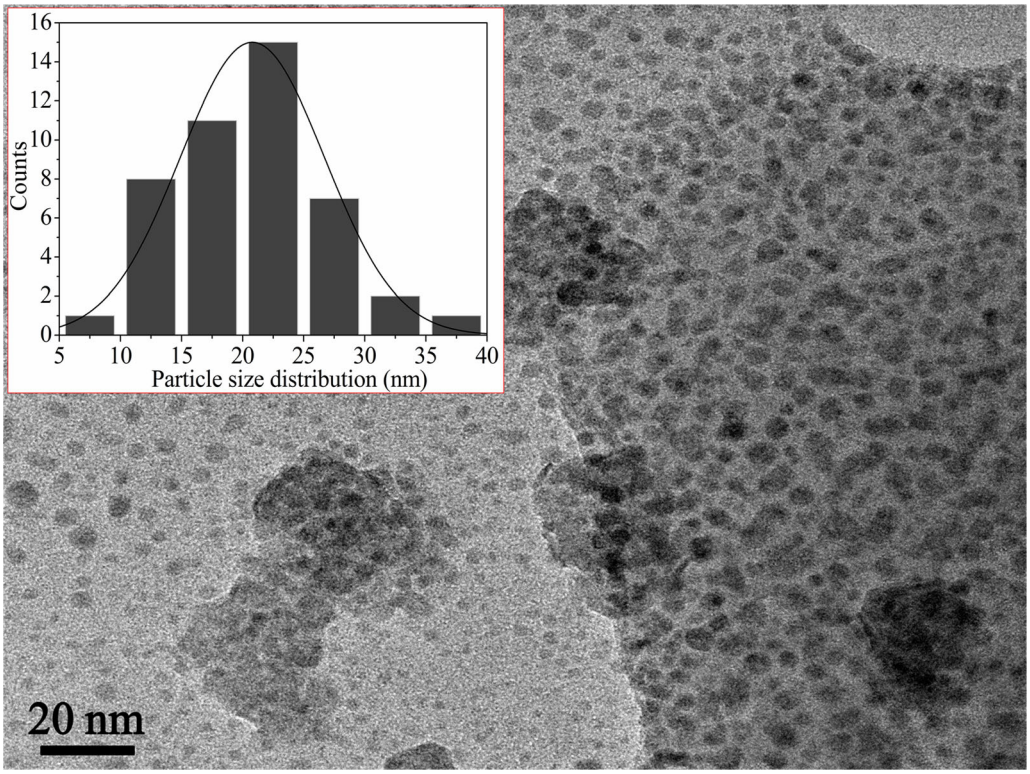

Figure 8. TEM image of the sample S_4 (0.8 M). The inset shows the corresponding particle size distribution histogram of the sample S_4.

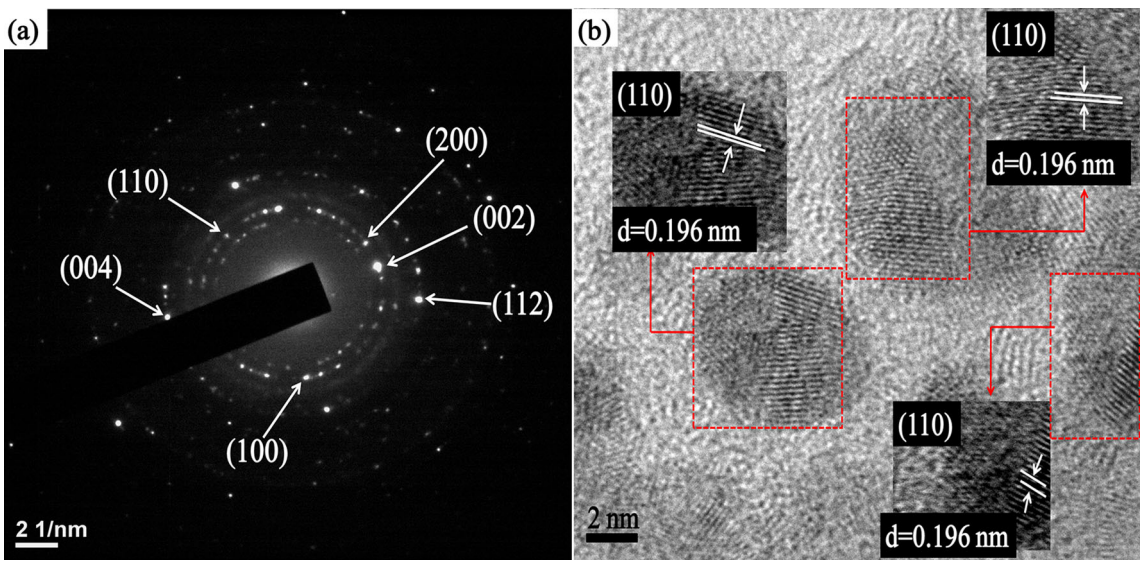

Figure 9. (**a**) The SAED pattern and (**b**) HRTEM image of sample S_4.

inscribes the genesis of uniformly distributed nearly cabbage-like structured particles in all the samples. In general, the nucleation and growth processes are prolonged, ensuring a well-defined matrix with strong coagulation of nanoparticles together. As a result, the multilayered nanoparticles could be assembled from the nanoparticle morphology. These multilayered nanoparticles were gradually moulded and they were partially formed as cabbage-like structure. With the increasing concentration, x, from 0.2 to 0.8, a denser distribution is observed over the surface. The average size among forty-three particles obtained from the distribution histogram calculated using the ImageJ software for the samples S_1, S_2, S_3 and S_4 are $\sim$222, 175, 155 and 123 nm, respectively (shown in figure 10b, d, f and h). SEM images show the larger particle size than the other sizes obtained from XRD and TEM. This mainly arises due

Table 3. Structural parameters of $Cd_xPb_{1-x}S$ thin films estimated from TEM, HRTEM images and SAED pattern.

Sample code	Concentration, x	Average particle size (nm)	HRTEM, d (nm)	Interplanar spacing, d (nm)	(hkl) planes	Phase assignment
S_2	0.2 M	~31	0.332	0.430	(110)	Tetragonal-PbS
				0.332	(002)	Hexagonal-CdS
				0.307	(200)	Tetragonal-PbS
				0.258	(211)	Tetragonal-PbS
				0.207	(110)	Hexagonal-CdS
				0.176	(112)	Hexagonal-CdS
				0.354	(100)	Hexagonal-CdS
				0.336	(002)	Hexagonal-CdS
S_4	0.8M	~21	0.196	0.307	(200)	Tetragonal-PbS
				0.207	(110)	Hexagonal-CdS
				0.176	(112)	Hexagonal-CdS
				0.165	(004)	Hexagonal-CdS

to the aggregate formation of more than four particles that patently increase the overall particle size. A gradual decrease in the average size of the particles is observed with the rise in concentration. The substitution of Cd ions bestows a retarding force on the particle boundaries. If the retarding force is greater than the driving force for particle growth due to Pb, the movement of the particle boundary is obstructed. This is in exchange for gradually decreasing particle size with increasing Cd concentrations. A substantial change in particle size is observed with a variation in concentration. Therefore, the size of the $Cd_xPb_{1-x}S$ particles can be superintended by tuning the concentration.

The EDX spectra of $Cd_xPb_{1-x}S$ thin films for the samples S_1, S_2, S_3 and S_4, respectively, along with the atomic percentage ratio S/(Cd+Pb) of the samples listed at the upper corner of the respective EDX images, is shown in figure 11. The EDX analysis confirms the presence of Pb, Cd and S in all the prepared films. EDX spectra also confirm the occurrence of Si, C, O and Au in the film samples. Si and O are present in the samples due to only glass substrates. The O is also present due to the deionized water solution used for films synthesis. Due to the carbon tape used to mount the samples in the instrument, C is present in all the film samples. All the film samples contain Au, which is associated with the prior gold coating to provide a better conducting surface at the time of analysis. It is observed that with the increasing x as concentration, Pb shows a decrease, and Cd shows a rising trend in the atomic list. The atomic percentage ratio of S/(Cd+Pb) for the samples S_1, S_2, S_3 and S_4 are 0.80, 0.81, 0.82 and 0.84, respectively. This result suggests that all the film samples approach stoichiometric ratio 1 with the increasing x.

3.3 *FTIR studies*

FTIR characterization is performed to study the formation and the associated functional groups present on the surface of the $Cd_xPb_{1-x}S$ samples. The FTIR spectra of $Cd_xPb_{1-x}S$ thin-film samples S_1 and S_4 prepared at the concentration of x = 0.2 and 0.8, respectively, are shown in figure 12. The peaks at 3400 cm^{-1} are very broad and arise due to the O–H stretching vibrations of water molecules present via the aqueous solvent used to prepare samples [51–53]. The small peaks at 2960 and 2820 cm^{-1} correspond to the Cd–O stretching vibrations [54]. The peaks that appeared at 2000 and 2140 cm^{-1} are due to the N–N stretching mode of diazomethane molecules that arises from Thiourea as an S^{2-} ion source [55–57]. The peaks at 1660 cm^{-1} correspond to the H–O–H bending vibration of water molecules [58]. The peaks at 1570 cm^{-1} arise due to the C=C stretching bond [59]. The peaks at 1400 cm^{-1} arise due to the C–H bending of the acetate group [60]. The frequency bands at 1050–1074–1100 cm^{-1} occurred due to the C–O stretching vibration of the acetate group present in the samples [61–63]. The peaks that appeared at 850–900 cm^{-1} correspond to the C–S bond due to the sulphide group present in Thiourea [64,65]. The prominent characteristic peak of Cd–S stretching vibrations are identified at 650–690 cm^{-1} [66,67]. The peaks at 420 cm^{-1} are assigned to the other most characteristic Pb–S vibrational bond [68].

3.4 *Optical studies*

The effects of variable x as concentration on the optical properties of $Cd_xPb_{1-x}S$ thin films were studied in the wavelength range of 450–1100 nm. Figure 13 shows the transmission spectra of $Cd_xPb_{1-x}S$ film samples S_1, S_2, S_3 and S_4. All the film samples possess good transmittance in the visible-light spectra and become more transparent in a wavelength longer than 600 nm. At the highest concentration x = 0.8, $Cd_xPb_{1-x}S$ thin films show maximum average transmittance of ~76%. The increase in concentration leads to a shift of absorption edges towards the shorter wavelength side, which results in the blue shift in the bandgap energy [69]. These shifts toward the shorter wavelength of the light implicit enlarging bandgap in the samples

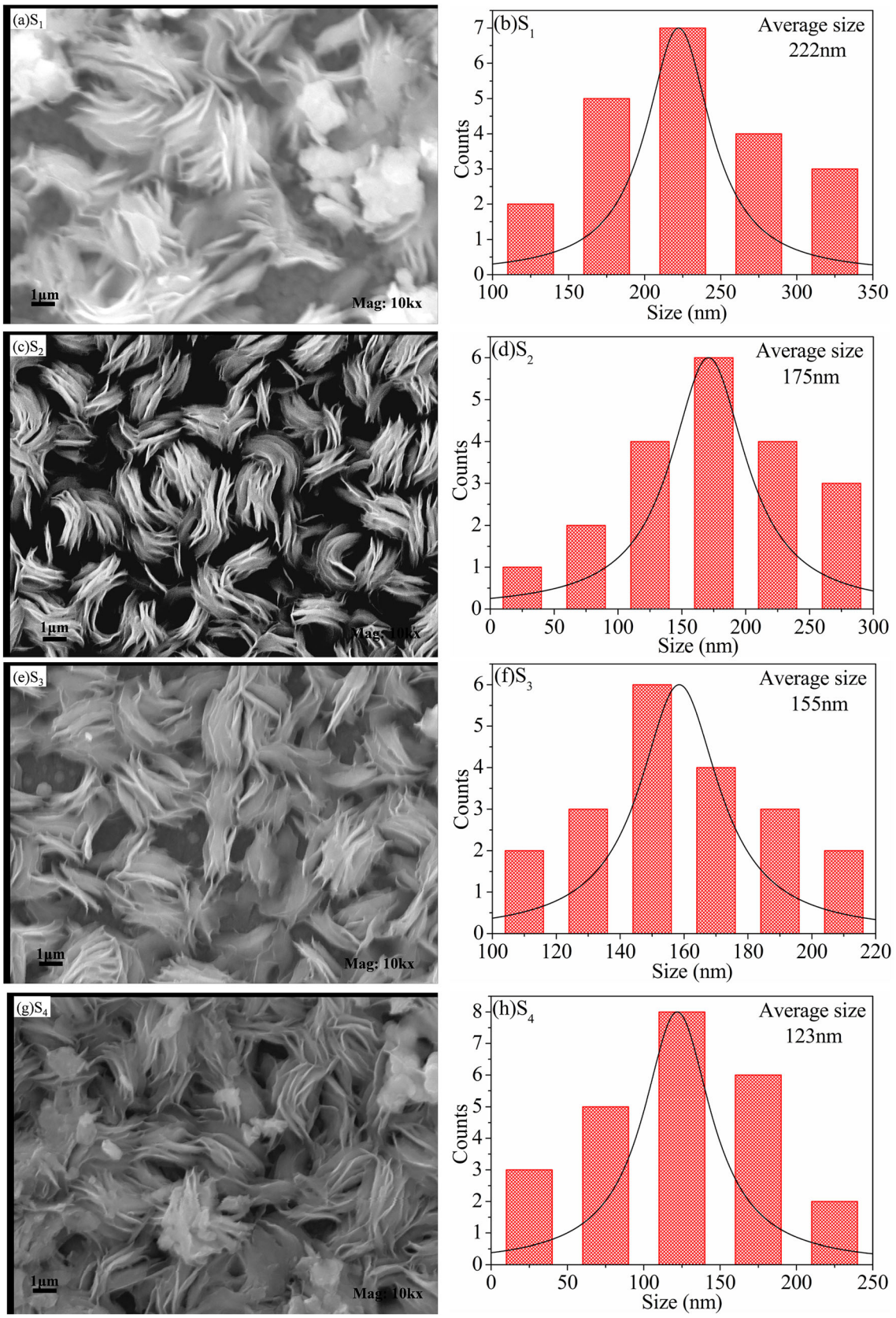

Figure 10. (**a**), (**c**), (**e**) and (**g**) SEM images, and (**b**), (**d**), (**f**) and (**h**) the corresponding particle size distribution histogram of $Cd_xPb_{1-x}S$ thin film samples for S_1, S_2, S_3 and S_4, respectively, prepared at different concentrations of *x*.

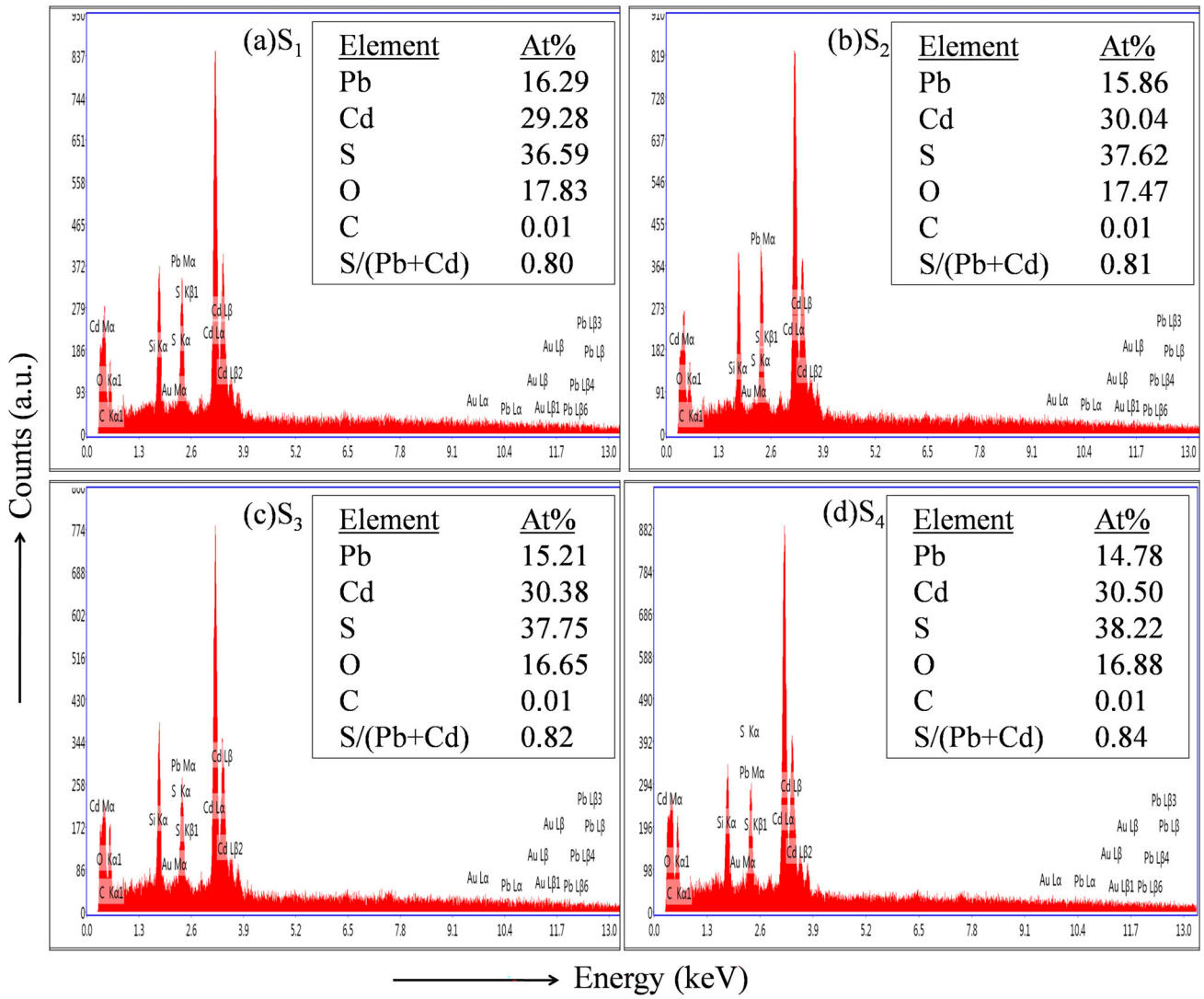

Figure 11. EDX spectra of $Cd_xPb_{1-x}S$ thin film samples: (**a**) S_1, (**b**) S_2, (**c**) S_3 and (**d**) S_4, respectively. Inset shows the atomic percentage ratios of S/(Pb + Cd).

simultaneously confirmed by studying the spectroscopic data via Tauc plots. From the results of the UV–visible, Tauc plots are drawn using the Tauc equation [70],

$$\alpha h\nu = A(h\nu - E_g)^{1/2}, \tag{3}$$

where, $h\nu$ is the photon energy, A is the Tauc slope, and α the absorption coefficient. From the transmission data, the absorption coefficient (α) of the $Cd_xPb_{1-x}S$ thin films is calculated using equation (4) [28],

$$\alpha = -\frac{1}{t}\ln T, \tag{4}$$

where, t is the thickness. The film's thickness was estimated by the Tolansky method using the equation, $t = \left(\frac{\Delta L}{L}\right)\lambda/2$, [71], where L is the fringe width or spacing, and $\Delta L/L$ is the fractional discontinuity of the fringe system. The thickness of the films decreases with the increase in x as concentration.

Figure 14 represents the plots of $(\alpha h\nu)^2$ *vs.* $h\nu$ for $Cd_xPb_{1-x}S$ thin films for S_1, S_2, S_3 and S_4, respectively. Inset of figure 14 shows the error bar of the band-gap graph. By extrapolating the straight linear portion of $(\alpha h\nu)^2$ *vs.* $h\nu$ plots to the energy axis at $\alpha = 0$, the bandgap values are estimated. The observed optical bandgap values of the samples S_1, S_2, S_3 and S_4 are ~2.05, 2.1, 2.18 and 2.24 eV, respectively, and are listed in table 4. The determined values of the bandgap are originated to be in between the bandgap values of bulk CdS (2.46 eV) and PbS (0.41 eV), which is expected from the formation of ternary $Cd_xPb_{1-x}S$ thin films. With the increase in x from 0.2 to 0.8, the bandgap values increase. The variation of bandgap energy with concentration x is shown in figure 15. The bandgap

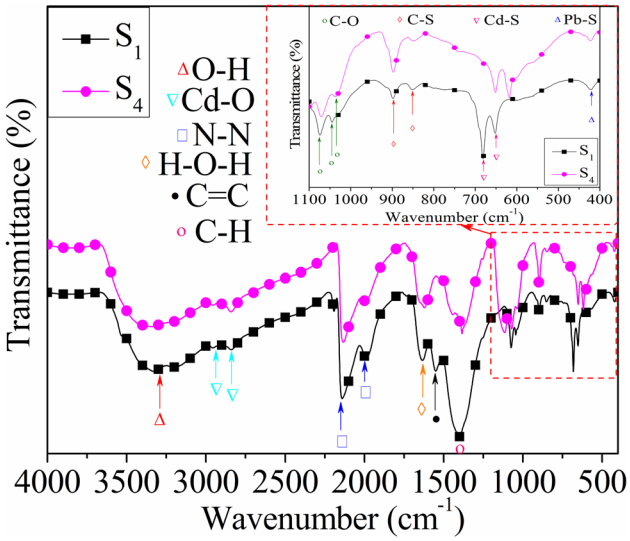

Figure 12. FTIR spectra of $Cd_xPb_{1-x}S$ thin film samples for S_1 (0.2 M) and S_4 (0.8 M). Inset shows the magnified area of wavenumber range of 400–1000 (cm^{-1}).

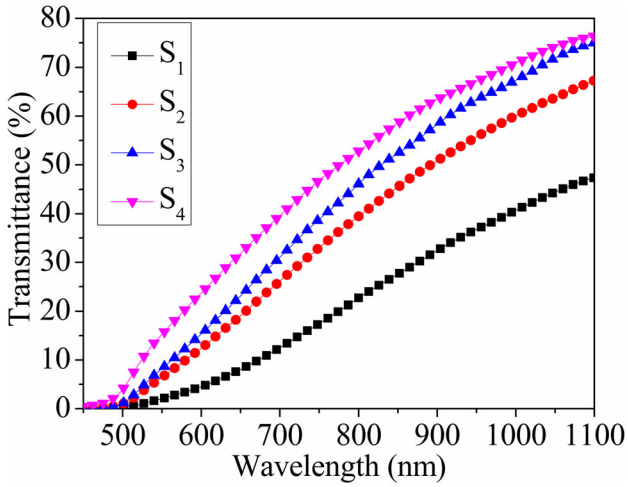

Figure 13. Plot of transmittance *vs.* wavelength of $Cd_xPb_{1-x}S$ thin film samples S_1, S_2, S_3 and S_4, respectively.

values widen as the crystallite size decreases from bulk to nano regime material [72]. Bandgap widening of nanomaterials is ascribed to the quantum mechanical effects of the low-dimensional crystallites. At these length scales, overlapping energy levels spread out to become more quantized, producing bandgap widening in the material. The XRD studies support the result.

Near the band edge, the absorption coefficient shows an exponential dependence on photon energy [73]. This exponential part, called the Urbach tail, appears as the materials have localized states in the extension of the bandgap [74]. The absorption coefficient and the photon energy are related by an empirical relation and known as Urbach equation (5) as [75],

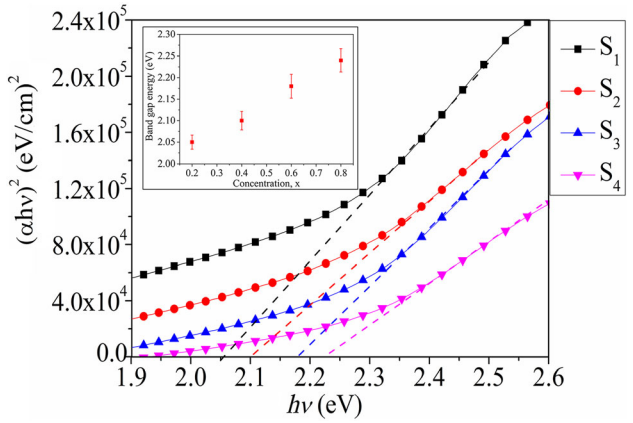

Figure 14. Plot of $(\alpha h\nu)^2$ *vs.* $h\nu$ for $Cd_xPb_{1-x}S$ thin film samples S_1, S_2, S_3 and S_4, respectively. Inset shows the error bar graph for banggap energy.

$$\alpha = \alpha_0 \exp\left(\frac{h\nu}{E_u}\right), \tag{5}$$

where, α_0 is a constant and E_u is the measurement of disorder in a crystalline material called Urbach energy. The lnα *vs.* $h\nu$ plots for the samples S_1, S_2, S_3 and S_4 prepared at different concentrations are shown in figure 16a. The slope of the straight line lnα *vs.* $h\nu$ plot is measured by least-square fitting. The reciprocal of the slope gives the corresponding Urbach energy of the $Cd_xPb_{1-x}S$ thin films, listed in table 4. The decrease in Urbach energy at higher concentrations indicates low structural disorder in the film samples. The variation of the Urbach energy with variable x as concentration is shown in figure 16b.

3.5 *Electrical studies*

Conductivity and resistivity are the constitutional property of a material. Electrical conductivity measures the amount of electrical current that a material can transfer. While the electrical resistivity estimates how much a material resists the flow of electricity. Across the film thickness, the current–voltage (I–V) characteristics of the $Cd_xPb_{1-x}S$ thin-film samples S_1, S_2, S_3 and S_4 prepared at different concentrations x is shown in figure 17a. From the I–V characteristic of the $Cd_xPb_{1-x}S$ films, it is observed that all the film samples show curve behaviour. The inverse of the slope of the I–V curve gives the resistance (R) of the films and is determined as in equation (6) [76],

$$R = \frac{1}{\text{Slope}}. \tag{6}$$

The resistivity (ρ) of the film samples was calculated using equation (7) [77],

$$\rho = \frac{RA}{t}, \tag{7}$$

Table 4. Optical and electrical parameter values of $Cd_xPb_{1-x}S$ thin films.

Sample code	Concentration, x	Thickness (nm)	Bandgap energy E_g (eV)	Urbach energy E_u (eV)	Electrical conductivity $\sigma \times 10^{-5}$ $(\Omega cm)^{-1}$
S_1	0.2	234	2.05	0.401	9.52
S_2	0.4	216	2.10	0.385	9.80
S_3	0.6	186	2.18	0.339	10.30
S_4	0.8	173	2.24	0.326	11.23

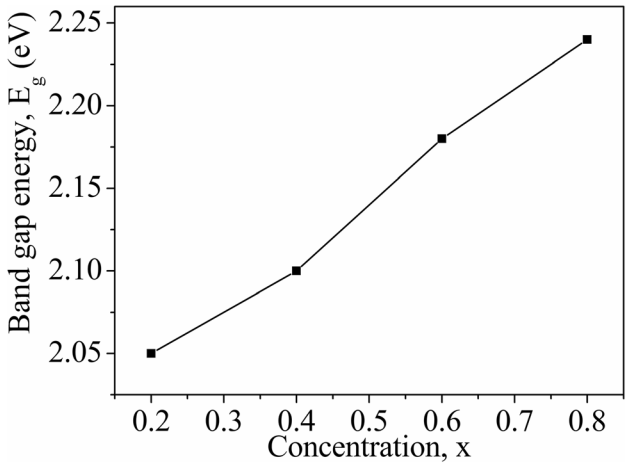

Figure 15. Plot of variation of bandgap energy (E_g) as a function of concentration, x, for $Cd_xPb_{1-x}S$ thin film samples S_1, S_2, S_3 and S_4, respectively.

where A is the active area of the thin film ($l \times t$ cm^2), $l = 0.2$ cm is the spacing between two probes, and t is the thickness. The resistivity of the film samples decreases with the increase in concentration x. The resistivity of the samples S_1, S_2, S_3 and S_4 are 1.05, 1.02, 0.97 and 0.89, respectively. These observed values of resistivity of the thin film samples are of the order of 10^4 Ωcm. Now, the electrical conductivity (σ) of the film samples were calculated from the resistivity data by using equation (8) [78],

$$\sigma = \frac{1}{\rho}. \tag{8}$$

The observed σ values are of the order of 10^{-5} $(\Omega cm)^{-1}$, listed in table 4. The electrical conductivity of the film samples increases with the increase in concentration and, the variation of σ with concentration x is shown in figure 17b. As the material shows semiconductor nature, we consider the prepared $Cd_xPb_{1-x}S$ thin films as n-type material. As earlier discussed in the section 3.4, it is found that the thickness of the films decreases with the increased concentration. Therefore, the surface of films will be smoother and also the films will be more compact. As a result, the conduction through the films increases. Belahssen *et al* [79] have reported a similar observation in their work.

3.6 *Characterization of heterojunction photovoltaic cells*

At present, the most promising techniques for photovoltaic cell implementation are based on photothermal and photovoltaic conversions. Photovoltaic cells are semiconductor

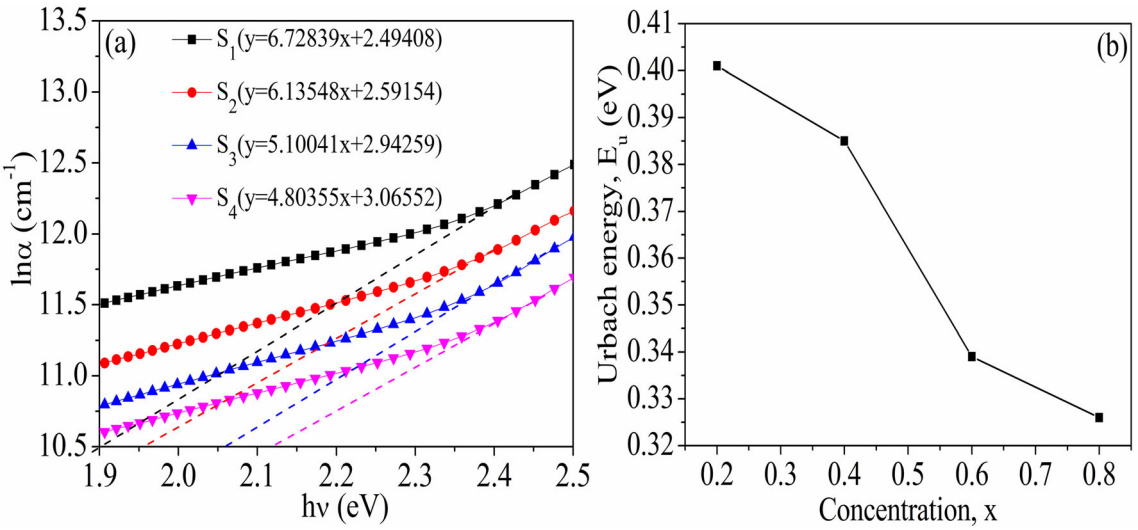

Figure 16. Plots of (**a**) lnα *vs. hv*, (**b**) variation of Urbach energy (E_u) as a function of concentration x, for $Cd_xPb_{1-x}S$ thin film samples S_1, S_2, S_3 and S_4, respectively.

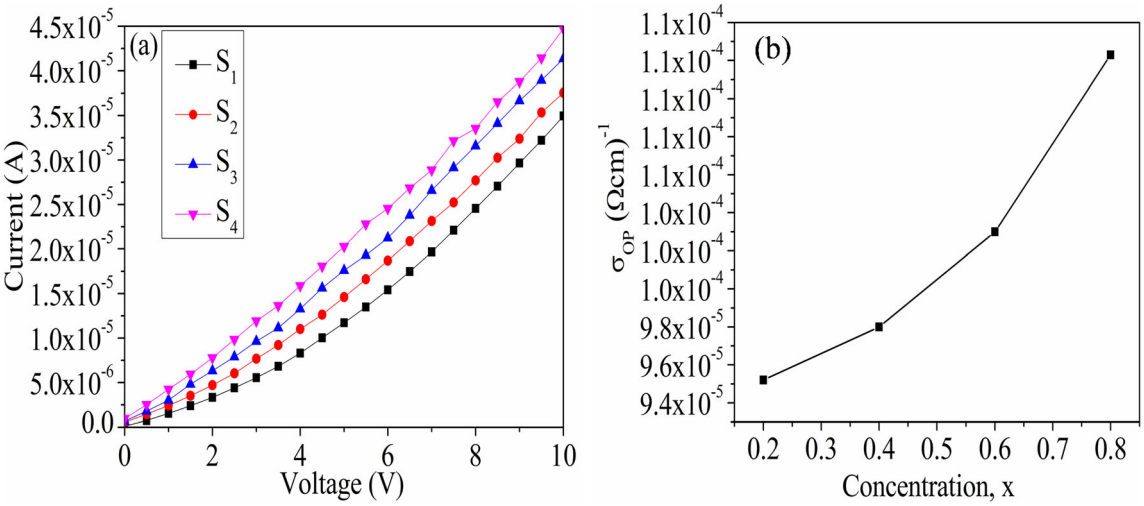

Figure 17. Plots of (**a**) current–voltage (*I–V*) characteristic, (**b**) variation of electrical conductivity (σ) as a function of concentration x, for $Cd_xPb_{1-x}S$ thin film samples S_1, S_2, S_3 and S_4, respectively.

Table 5. Heterojunction photovoltaic cell parameters.

Cell code	Fabricated heterojunction photovoltaic cell structures	Short-circuit current, J_{sc} (mA cm^{-2})	Open-circuit voltage, V_{oc} (mV)	Fill factor, FF (%)	Conversion efficiency, η (%)
Cell-1	ITO/$Cd_xPb_{1-x}S$/CdTe/Al	24.9	620	53	3.37
Cell-2	ITO/$Cd_xPb_{1-x}S$/CdSe/Al	21.7	550	49	2.21

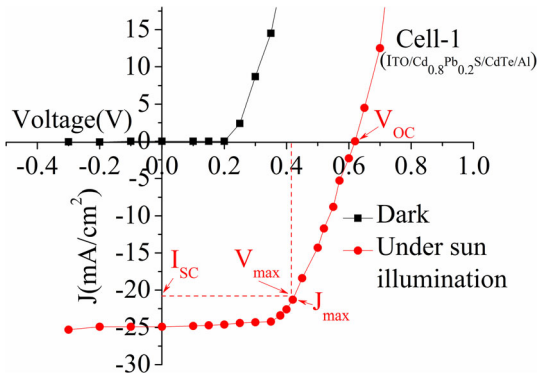

Figure 18. Current–voltage (*J–V*) characteristics of fabricated Cell-1 (ITO/$Cd_{0.8}Pb_{0.2}S$/CdTe/Al) in dark and under illumination.

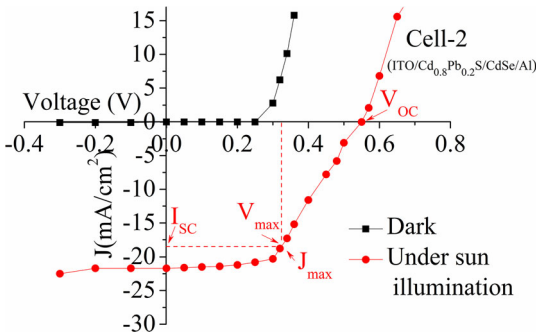

Figure 19. Current–voltage (*J–V*) characteristics of fabricated Cell-2 (ITO/$Cd_{0.8}Pb_{0.2}S$/CdSe/Al) in dark and under illumination.

devices that generate electric power when exposed to electromagnetic radiation. At higher concentration of Cd, i.e., at $x = 0.8$ M, $Cd_xPb_{1-x}S$ thin film has high transmittance and high bandgap energy E_g. Therefore, $Cd_{0.8}Pb_{0.2}S$ thin films are considered as a most suitable window layer for photovoltaic cells. Hence, current–voltage (*J–V*) characteristic have been plotted for heterojunction structures, in which $Cd_{0.8}Pb_{0.2}S$ thin films were considered as a window layer with two absorber layers CdTe and CdSe. ITO/$Cd_{0.8}Pb_{0.2}S$/CdTe/Al and ITO/$Cd_{0.8}Pb_{0.2}S$/CdSe/Al heterojunction structures had been fabricated, and coded as Cell-1 and Cell-2, respectively, listed in table 5. $Cd_{0.8}Pb_{0.2}S$ window layer (n-type) absorbed the incident photons and transmitted them into CdTe and CdSe absorber layer (p-type), leading to photoelectron generation.

The thickness of $Cd_{0.8}Pb_{0.2}S$ window layer coated over the ITO glass substrate using suitable mask was estimated by weighing method. The difference in weight of the ITO-coated glass substrate before and after deposition of $Cd_{0.8}Pb_{0.2}S$ thin film was taken by electronic balance. Using equation (9), the thickness of the film was obtained as,

$$d = \frac{m}{\Delta \rho A}, \tag{9}$$

where m is the mass of the deposited film in gram, A is the area of the film in cm^2, and ρ is the density of the film material in g cm^{-3}. The thickness of the ITO/$Cd_{0.8}Pb_{0.2}S$ was ~229 nm. The absorber layers thickness were estimated by the Tolansky method using the equation, $t = \left(\frac{\Delta L}{L}\right)\lambda/2$, where L is the fringe width or spacing, and $\Delta L/L$ (~4.01) is the fractional discontinuity of the fringe system. The thickness of both the absorber layer CdTe is ~994 nm and CdSe is ~834 nm.

The most key performance characteristics parameters of a photovoltaic cell include open-circuit voltage (V_{oc}), short-circuit current (I_{sc}), fill factor (FF) and conversion efficiency (η). The voltage at which no current flows through a photovoltaic cell is called open circuit voltage, V_{oc}. It is the maximum voltage accessible from the photovoltaic cell. Only the short-circuit (I_{sc}) flows through the photovoltaic cell at zero voltage. The short-circuit current acts for the maximum current that could be attained in a photovoltaic cell [80]. The solar cell parameters can be determined from the J–V characteristics of Cell-1 and Cell-2 in dark and under 100 mW cm^{-2} illuminations. Figure 18 shows the J–V characteristics of fabricated Cell-1 ($Cd_{0.8}Pb_{0.2}S$/CdTe) in dark and under sun illumination. Figure 19 shows the J–V characteristics of fabricated Cell-2 ($Cd_{0.8}Pb_{0.2}S$/CdSe) in dark and under sun illumination. At the knee of the J–V curve, the maximum power (P_{max}) for both the cells is measured by equation (10) [81],

$$P_{max} = J_m \times V_m, \tag{10}$$

where V_m is the maximum cell voltage, and J_m is the maximum cell current. The calculated P_{max} for the cell structures Cell-1 and Cell-2 are 7,161 and 5,428 mW, respectively.

Another important parameter, the FF, which determines the quality of a photovoltaic cell, measures the squareness of I–V characteristics under illumination. It can be explained as the ratio of the rectangle area corresponding to the actual maximum power output from the device to the area of the rectangle corresponding to the maximum permissible power output from the device. FF of the photovoltaic cells is given by equation (11) [82],

$$\mathrm{FF} = \frac{P_{max}}{J_{SC} \times V_{OC}} = \frac{J_m \times V_m}{J_{SC} \times V_{OC}}, \tag{11}$$

where J_{sc} is the short-circuit current and V_{oc} is the open-circuit voltage of the cells. The values of FF of the fabricated cell structures Cell-1 and Cell-2 are found to be 0.53 or 53% and 0.49 or 49%, respectively.

The other most important parameter of a photovoltaic cell's ultimate function is its conversion efficiency (η). The percentage of the solar energy converted by a photovoltaic device into useable electricity is the conversion efficiency of the photovoltaic cell. The efficiency of the photovoltaic cell is the power density delivered at the operating point, and is given by equation (12) [83],

$$\eta = \frac{P_{max}}{P_{in}} = \frac{J_{SC} \times V_{OC}}{P_{in}}\ \mathrm{FF}, \tag{12}$$

where P_{in} is the input power. The calculated conversion efficiency (η) values of the heterojunction cells of Cell-1 and Cell-2 are 3.37 and 2.21%, respectively. From the result, it is clearly observed that the value of 'η' of Cell-1 ($Cd_{0.8}Pb_{0.2}S$/CdTe) is more than that of Cell-2 ($Cd_{0.8}Pb_{0.2}S$/CdSe). Therefore, it can be summarized that $Cd_{0.8}Pb_{0.2}S$/CdTe has better photovoltaic performance than $Cd_{0.8}Pb_{0.2}S$/CdSe cell. All the observable values of J_{sc}, V_{oc}, FF and η are listed in table 5.

4. Conclusions

The variation in the concentration causes significant changes in the synthesized $Cd_xPb_{1-x}S$ ternary films' structural, morphological, optical and electrical properties. XRD, HRTEM and SAED pattern studies indicate the presence of hexagonal and tetragonal phase structures of $Cd_xPb_{1-x}S$ thin films. The average crystallite size calculated from both XRD and W–H plots decreases with the increase in concentration. SEM images also indicate the decrement of particle size with increasing concentration. The presence of different functional groups and the formation of the bonds between Pb–S and Cd–S were confirmed by FTIR analysis. The transmittance and the optical bandgap energy increases, while the Urbach energy decreases with the increased concentration. The electrical resistivity and conductivity of the $Cd_xPb_{1-x}S$ thin films are of the order of 10^4 (Ωcm) and 10^{-5} $(\Omega cm)^{-1}$, respectively. The obtained results implicate that the present analysis of $Cd_xPb_{1-x}S$ thin films is a superlative candidate as a window layer for photovoltaic cells. The efficiencies of the fabricated heterojunction $Cd_xPb_{1-x}S$/CdTe and $Cd_xPb_{1-x}S$/CdSe are estimated to be 3.21 and 2.19%, respectively.

Acknowledgements

We acknowledge SAIF, Gauhati University, Guwahati (India), for providing PXRD facilities, and SAIF-NEHU, Shillong, Meghalaya (India) for TEM, HRTEM and SAED facilities. We acknowledge the CSIC, Dibrugarh University, Dibrugarh (India), for providing the SEM and EDX facilities, and SAIC, Tezpur University (India), for supplying FTIR facilities. We also acknowledge the Department of Chemistry, Dibrugarh University, Dibrugarh (India), for Source Meter facility to record I–V characteristics.

References

[1] Shu T, Zhou Z M, Wang H, Liu G H, Xiang P, Rong Y G *et al* 2011 *J. Nanosci. Nanotechnol.* **11** 9645

[2] Choubey R K, Desai D, Kale S N and Kumar S 2016 *J. Mater. Sci.: Mater. Electron.* **27** 7890
[3] Barote M A, Kamble S S, Deshmukh L P and Masumdar E U 2013 *Ceram. Int.* **39** 1463
[4] Muradov M B, Gahramanli L R, Balayeva O O, Nasibov I N, Eyvazova G M, Amiraslanov I R *et al* 2020 *Results Phys.* **18** 103280
[5] Vankhade D and Chaudhuri T K 2020 *J. Appl. Phys.* **127** 175107
[6] Patel J, Mighri F, Ajji A, Tiwari D and Chaudhuri T K 2014 *Appl. Phys. A* **117** 179
[7] Ali S M, AlGarawi M S, Aldawood S, Al Salman S A and AlGamdi S 2020 *Radiat. Phys. Chem.* **171** 108732
[8] Liu M, Zhan Q, Li W, Li R, He Q and Wang Y 2019 *J. Alloys Compd.* **792** 1000
[9] Fouda A N, Marzook M, AbdEI-Khalek H M, Ahmed S, Eid E A and Basaty A B E I 2017 *Silicon* **9** 809
[10] Hone F G, Dejene F B and Koao L F 2021 *Indian J. Phys.* **95** 1763
[11] Paulraj K, Ramaswany S, Shkir M, Yahia J S, Hamdy M S and Faify S A 2020 *J. Mater. Sci. Mater. Electron.* **31** 1817
[12] Seghaier S, Kamoun N, Brini R and Amara A B 2006 *Mater. Chem. Phys.* **97** 71
[13] Yücel E and Yücel Y 2017 *Ceram. Int.* **43** 407
[14] Zellagui R, Dehdouh H, Adnane M, Akhtar M S and Saeed M A 2020 *Optik* **207** 164377
[15] Barman J, Borah J P and Sarma K C 2008 *Chalcogenide Lett.* **5** 265
[16] Qin Z Q and Zhang F J 2013 *Appl. Surf. Sci.* **285** 912
[17] Orlianges J C, Champeaux C, Dutheil P, Catterinot A and Mejean T M 2011 *Thin Solid Films* **519** 7611
[18] Ma L, Ali X and Wu X 2017 *J. Alloys Compd.* **691** 399
[19] Kamruzzaman M, Dutta R and Poddar J 2012 *Semiconductors* **46** 957
[20] Gogoi L, Chaliha S and Saikia P K 2019 *AIP Conf. Proc.* **2100** 020034
[21] Boyle D S, O'Brien P, Otway D J and Robbe O 1999 *J. Mater. Chem.* **9** 725
[22] Obaid A S, Mahdi M A, Hassan Z and Bououdina M 2012 *Mater. Sci. Semicond. Process.* **15** 564
[23] Jana S, Thapa R, Maity R and Chattopadhyay K K 2008 *Physica E* **40** 3121
[24] Mukhamale S V and Chaure N B 2013 *AIP Conf. Proc.* **1512** 388
[25] Nair S B, Abraham A, Pradeep B, Shripathi T, Ganesan V and Philip R R 2014 *AIP Conf. Proc.* **1620** 511
[26] Forostyanaya N A, Maskaeva L N, Smirnova Z I, Santra S, Zyryanov G V and Markovet V F 2018 *Thin Solid Films* **657** 101
[27] Deo S R, Singh A K, Desmukh L, Paliwai L J and Singh R S 2015 *Optik* **126** 2311
[28] Anbarasi M, Nagarethinam V S, Raskaran R and Narasimman V 2016 *Pac. Sci. Rev. A.: Natural Sci. Eng.* **18** 72
[29] Gogoi L, Chaliha S, Borah D J and Saikia P K 2021 *Bull. Mater. Sci.* **44** 225
[30] Sinha T, Verma L and Khare A 2020 *Appl. Phys. A* **126** 867
[31] Simda A, Zaaboub Z, Bel Haj Mohamed N, Hassen M, Laatar F, Maaref H *et al* 2018 *J. Lumin.* **194** 686
[32] Baines T, Zoppi G, Bowen L, Shavey T P, Mariotti S, Durose K *et al* 2018 *Sol. Energy Mater. Sol. Cells* **180** 196
[33] Chander S and Dhaka M S 2016 *J. Mater. Sci.: Mater. Electron.* **27** 11961
[34] Munshi A H, Kephart J M, Abbas A, Danielson A, Gelinas G, Beaudry J N *et al* 2018 *Sol. Energy Mater. Sol. Cells* **186** 259
[35] Durose K, Edwards P R and Halliday D P 1999 *J. Cryst. Growth* **197** 733
[36] Spalatu N and Krunks M 2017 *Thin Solid Films* **633** 106
[37] Patel S L, Kaushalya H, Chander S, Purohit A, Kannan M D and Dhaka M S 2019 *Opt. Mat.* **89** 42
[38] Patel S L, Purohit A, Chander S, Kannan M D and Dhaka M S 2018 *Vacuum* **153** 43
[39] Ojo A A and Dharmadasa I M 2018 *Sol. Energy* **170** 398
[40] Patel S L, Kaushalya H, Chander S, Kannan M D and Dhaka M S 2019 *J. Mater. Sci.: Mater. Electron.* **30** 20840
[41] Portillo-Moreno O, Lima-Lima H, Ramirez-Falcon V, Martinez-Juarez J, Juarez-Diaz G, Lozada-Morales R *et al* 2006 *J. Electrochem. Soc.* **153** G926
[42] Chavez Portillo M, Portillo Moreno O, Gutierrez Perez R, Palomino Merino R, Santiesteban Juarez H, Tehuacanero Cuapu S *et al* 2017 *Mater. Sci. Semicond. Process.* **72** 22
[43] Portillo-Moreno O, Gutierrez Perez R, Chavez Portillo M, Chaltel Lima L, Hernandez Tellez G and Rubio Rosas E 2016 *Optik* **127** 10273
[44] Vineeshkumar T V, Ritesh Raj D, Prasanth S, Unnikrishnan N V, Philip R and Sudarsanakumar C 2014 *Opt. Mater.* **37** 439
[45] Patterson A I 1939 *Phys. Rev.* **56** 978
[46] Senthil M S, Saravanan K, Susila S P and Kumaresh Babu S P 2011 *Phys. B: Conden. Matter.* **406** 165
[47] Zak A K, Abd Majid W H, Abrishami M E and Yousefi R 2011 *Solid State Sci.* **13** 251
[48] Solanki R G, Rajaram P and Bajpai P 2018 *Indian J. Phys.* **92** 595
[49] Sethilkumar V, Vickraman P, Jayachandran M and Sanjeeviraja C 2010 *J. Mater. Sci.: Mater. Electron.* **21** 343
[50] Prabhu R R and Abdul Khadar M 2008 *Bull. Mater. Sci.* **31** 511
[51] Ayodhya D and Veerabhadram G 2019 *J. Sci.: Adv. Mater. Devices* **4** 381
[52] Patil S V, Deshmukh P R and Lokhande C 2011 *Sens. Actuators B* **156** 450
[53] Narasimman V, Nagarethinam V S, Usharani K and Balu A B 2016 *Int. J. Thin Film Sci. Tec.* **5** 17
[54] Bora J, Borthakur A, Arandhara G and Saikia P K 2021 *Thin Solid Films* **734** 138847
[55] Khilfi M, Paillous P, Bruston P and Raulin F 1996 *Icarus* **124** 318
[56] Crawford B L Jr, Fletcher W H and Ramsay D A 1951 *J. Chem. Phys.* **19** 406
[57] Vogt J and Winnewisser M 1984 *Chem. Phys.* **83** 309
[58] Muthukumaran S and Ashok Kumar M 2013 *Mater. Lett.* **93** 223
[59] Gahramanli L, Muradov M, Kukovecz A, Balayeva O and Eyvazova G 2020 *Inorg. Nano. Met. Chem.* **50** 808
[60] Farazin J, Givi G P and Kalandaragh Y A 2019 *Physica B: Condens. Matter* **564** 94
[61] Pawar S B, Shaikh J S, Devan R S, Ma Y R, Haranath D, Bhosale P N *et al* 2011 *Appl. Surf. Sci.* **258** 1869
[62] Aziz S B, Rasheed M A, Saeed S R and Gh Abdullah O 2017 *Int. J. Electrochem. Sci.* **12** 3263
[63] Heiba Z K, Mohamed M B, Abdellatief M and Albassam A A 2020 *Appl. Phys. A* **126** 518

[64] Sharma S, Reddy A V D, Jayarambabu N, Kumar N V M, Saineetha A, Kailasa S *et al* 2020 *Mater. Today Proc.* **26** 162
[65] Ranjan R and Sinha A S K 2019 *Int. J. Hydrogen Energy* **44** 5955
[66] Poornaprakash B, Chalapathi U, Kumar M, Subramanyam K, Vattikuti S V P, Reddy M S P *et al* 2020 *Ceram. Int.* **46** 21728
[67] Sabah A, Siddiqi S A and Ali S 2010 *World Acad. Sci Eng. Technol.* **69** 82
[68] Rajathi S, Kirubavathi K and Selvaraju K 2017 *J. Taibah Univ. Medical Sci.* **11** 1296
[69] Munna F T, Chelvanathan P, Sobayel K, Nurhafiza K, Sarkar D K, Nour M *et al* 2020 *Optik* **218** 165197
[70] Isik M, Gulu H H, Delice S, Parlak M and Gasanly N M 2019 *Mater. Sci. Semicond. Process.* **93** 148
[71] Tolansky S 1970 *Phys. Today* **23** 95
[72] Yadav I and Ahlawat D S 2020 *Mater. Sci. Eng. B* **252** 114450
[73] Dey P P and Khare, 2010 Mater. *Res. Bull.* **84** 105
[74] Bashar M S, Matin R, Sultana M, Siddika A, Rahman M, Gafur M A *et al* 2020 *J. Theor. Appl. Sci.* **14** 53
[75] Urbach F 1953 *Phys. Rev.* **92** 1324
[76] Arandhara G and Saikia P K 2021 *Physica B Condens. Matter* **610** 412924
[77] Chavan A R, Birajdar S D, Chilwar R R and Jadav K M 2018 *J. Alloys Compd.* **735** 2287
[78] Kittel C 2004 *Introduction to solid state physics* 8th edn (Wiley) p 25
[79] Belahssen O, Benramache S and Benhaoua B 2015 *27th International Conference on Micoelectronics (ICM)* 182
[80] Neville R 1995 *Solar energy conversion: the solar cell* (Amsterdam: Elsevier Science)
[81] Kosyachenko L A 2015 *Solar cells: new approaches and reviews* (London: IntechOpen)
[82] Lilhare D and Khare A 2020 *Opt. Mater.* **108** 110385
[83] Gode F and Unlu S 2019 *Mater. Sci. Semicond. Process.* **90** 92